POLITECNICO
MILANO 1863

SCUOLA DI INGEGNERIA INDUSTRIALE
E DELL'INFORMAZIONE

A Computational Framework for Longitudinal Airway Analysis in Chronic Hypersensitivity Pneumonitis

TESI DI LAUREA MAGISTRALE IN
BIOMEDICAL ENGINEERING - INGEGNERIA BIOMEDICA

Author: **Martino Ghezzi**

Student ID: 10726930
Advisor: Francesca Pennati
Co-advisor: Andrea Aliverti
Academic Year: 2024-25

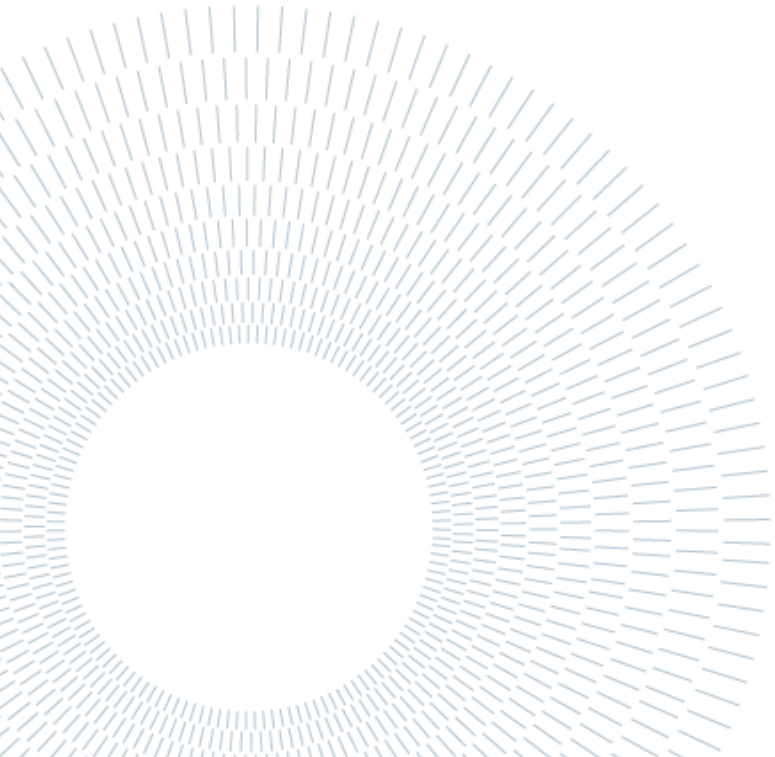

Abstract

Chronic Hypersensitivity Pneumonitis (CHP) is a heterogeneous interstitial lung disease with variable inflammatory and fibrotic remodelling [1]. Clinical follow-up mainly relies on spirometry, especially forced vital capacity (FVC), which is global, not region-specific [2]. This thesis presents a reproducible pipeline to quantify longitudinal airway geometric changes from chest high-resolution CT (HRCT) and relate them to functional and parenchymal variations in CHP.

The workflow includes: (1) segmentation of airway tree, lungs and lobes; (2) extraction of airway geometric measurements; (3) longitudinal registration; (4) statistical analysis on a CHP cohort. Airways were segmented with a pretrained "ATM22 Challenge" model (team Yang) [3] and lungs/lobes with TotalSegmentator [4]. A validated measurement tool was extended for deeper trees. Registration used whole-lung affine pre-alignment followed by deformable refinement on saturated-airway HRCTs. The clinical CHP dataset comprised longitudinal inspiratory non-contrast HRCTs and spirometry: each longitudinal pair was grouped by ΔFVC into Improving (>+5%), Stable (-5% to +5%) and Worsening (<−5%). For each group, intensity and geometrical changes were calculated at global (whole-lung) and local (lobar) level.

Registration validation achieved a median target registration error on bifurcation points of 1.50 mm (IQR 0.96-2.07 mm). Global mean density variations clearly separated groups (negative in Improving, near-zero in Stable, positive in Worsening), whereas global airway geometry alone was less discriminative. Lobar analyses instead showed stronger links between intensity and geometrical changes: Improving subjects exhibited dimensional increases with decreasing density; Stable showed limited mixed

changes; Worsening displayed heterogeneous patterns consistent with fibrotic narrowing and traction bronchiectasis.

Overall the pipeline enables quantitative assessment of airway remodelling, supporting CHP monitoring. Future work should include larger standardized cohorts, finer regional stratification and integration with automated pattern-recognition methods for improved phenotyping and prognostic stratification.

Key-words: airways; chronic hypersensitivity pneumonitis; registration; segmentation; longitudinal study.

Abstract in italiano

La Polmonite da Ipersensibilità Cronica (CHP) è una patologia interstiziale polmonare eterogenea con rimodellamento infiammatorio e fibrotico variabile [1]. Il follow-up clinico si basa sulla spirometria, in particolare sulla capacità vitale forzata (FVC), con indicatori globali e non regionali [2]. Questa tesi propone una pipeline per quantificare le variazioni geometriche longitudinali delle vie aeree su TC ad alta risoluzione (HRCT) e correlarle a variazioni funzionali e parenchimali nella CHP.

Il workflow include: (1) segmentazione di vie aeree, polmoni e lobi; (2) estrazione di misure geometriche; (3) registrazione longitudinale; (4) analisi statistica su una coorte CHP. Le vie aeree sono state segmentate con un modello vincitore della "ATM22 Challenge" (team Yang) [3] e polmoni/lobi con TotalSegmentator [4]. Un algoritmo di misura validato è stato integrato per gestire alberi più profondi. La registrazione ha usato un pre-allineamento affine sull'intero polmone, seguito da una registrazione deformabile su HRCT con vie aeree saturate. Il dataset clinico comprendeva HRCT inspiratorie longitudinali senza contrasto e spirometrie: ogni coppia longitudinale è stata suddivisa per ΔFVC in Improving (>+5%), Stable (da -5% a +5%) e Worsening (<−5%). Variazioni medie di intensità e geometriche sono state calcolate a livello globale (polmone) e locale (lobi).

La validazione ha ottenuto un target registration error mediano sui punti di biforcazione di 1.50 mm (IQR 0.96-2.07 mm). Le variazioni globali di densità hanno separato i gruppi (< 0 negli Improving, ~0 negli Stable, > 0 nei Worsening), mentre quelle geometriche erano meno discriminanti. L'analisi lobare ha mostrato legami più forti tra intensità e geometria: aumenti dimensionali con densità ridotte negli

Improving; cambiamenti limitati negli Stable; pattern variabili nei Worsening compatibili con restringimenti fibrotici e bronchiectasie da trazione.

In sintesi, la pipeline permette analisi quantitative sul rimodellamento delle vie aeree supportando il monitoraggio della CHP. Futuri sviluppi includono coorti più ampie, stratificazione più fine e inclusione di pattern-recognition per migliorare la stratificazione.

Parole chiave: vie aeree; polmonite da ipersensibilità cronica; registrazione; segmentazione; studio longitudinale.

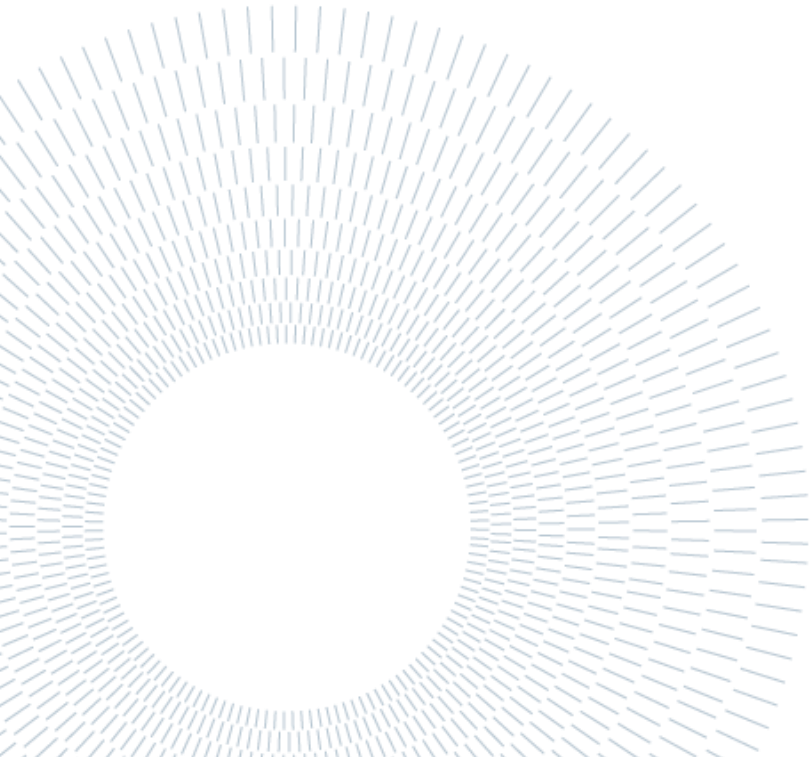

Contents

1 Introduction

1.1. Anatomy of the Respiratory System

In humans and many other species, the lungs are the central organ of the respiratory system. Their primary function is to take up oxygen from ambient air and deliver it to the bloodstream, while removing carbon dioxide for exhalation [5] [6].

From the functional perspective, the respiratory system is commonly divided into two zones:

- The conductive zone, which provides a pathway for airflow and extends from the nose to the terminal bronchioles.
- The respiratory zone, where the gas exchange with blood happens and it includes the alveolar ducts and the alveoli [7] [8].

From the anatomical point of view, instead, it can be divided into upper tract and lower tract, according to the location of the organs, depending on whether structures lie outside or within the thorax respectively. The upper airways extend from mouth and nose to the larynx, while the lower airways run from the trachea to the alveoli as shown in Figure 1.1: in this thesis, the analysis focuses on the lower airways and in particular on the tracheobronchial tree [7][41].

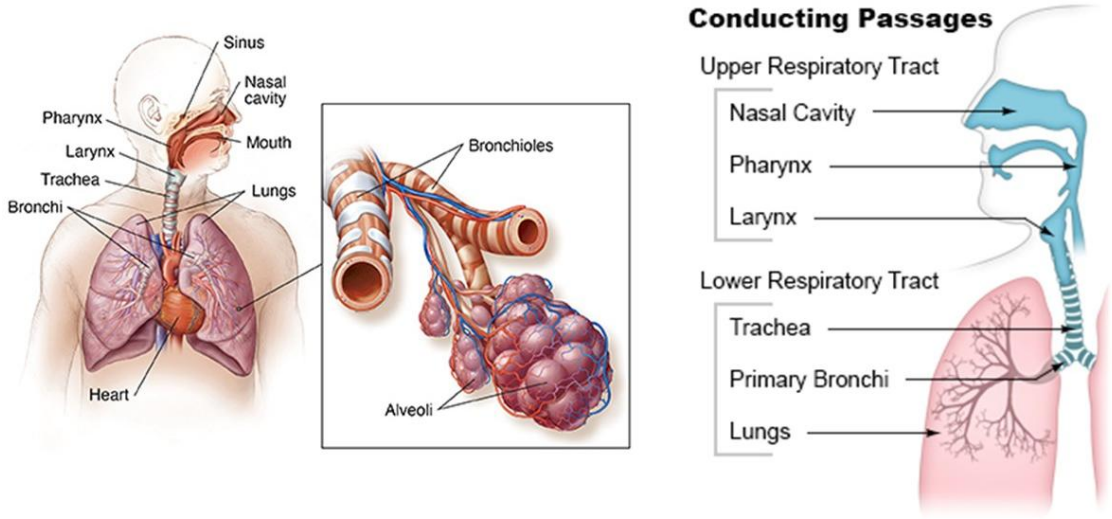

Figure 1.1 – Anatomy of the respiratory system [a][b].

1.1.1. Upper airways

Nasal cavity. It lies in and posterior to the external nose, and it is the first region in which inspired air passes. It is divided into two parts by the nasal septum, and they are delimited laterally by 3 conchae (superior, middle, and inferior) and the nasal mucosa, together with sinuses in the surrounding bones. These regions humidify and warm air, while removing contaminated mucus with ciliated cells. Additionally, its structure makes the airflow turbulent to facilitate proper humidification and filtration [7][41].

Pharynx. It is a tubular passage of skeletal muscle that connects the nasal cavity (nasopharynx) and mouth (oropharynx) to the larynx and esophagus (laryngopharynx): this is why it allows airflow in some regions, and it is a passage for both food and air in others [7].

Larynx. It is located between the pharynx and the trachea, allowing air passage. It is composed of 9 cartilages and has a fundamental role also in swallowing, by covering the laryngeal inlet during this process, as well as in voice production [41].

1.1.2. Lower airways

After initial filtration, humidification, and warming in the upper airways, inspired air travels through the tracheo-bronchial tree [6]. The first segment is the trachea, a passage made up of ciliated pseudostratified columnar cells over C-shaped cartilage, which bifurcates at the level of the carina into the two main bronchi. Anatomically, the two lungs can be divided into five distinct areas called lobes, which can be easily identified by fissures separating them. These regions are reached by five lobar bronchi: the right bronchus, shorter and more vertical, gives rise to three lobar bronchi supplying the superior, middle, and inferior right lobes; the left bronchus, on the other hand, gives rise to two lobar bronchi supplying the superior and inferior left lobes. Each lobar bronchus, in turn, subdivides into segmental bronchi that ventilate the broncho-pulmonary segments of the lobe, which are 10 in the right lung and 8 in the left lung, and are not anatomically defined as the lobes. As the airway tree continues to subdivide, cartilage disappears, epithelial cells become cuboidal, and airway dimensions decrease as shown in Figure 1.2. Smooth muscle becomes progressively more prominent and functionally relevant as cartilage disappears, forming a continuous layer in the terminal bronchioles [41][7].

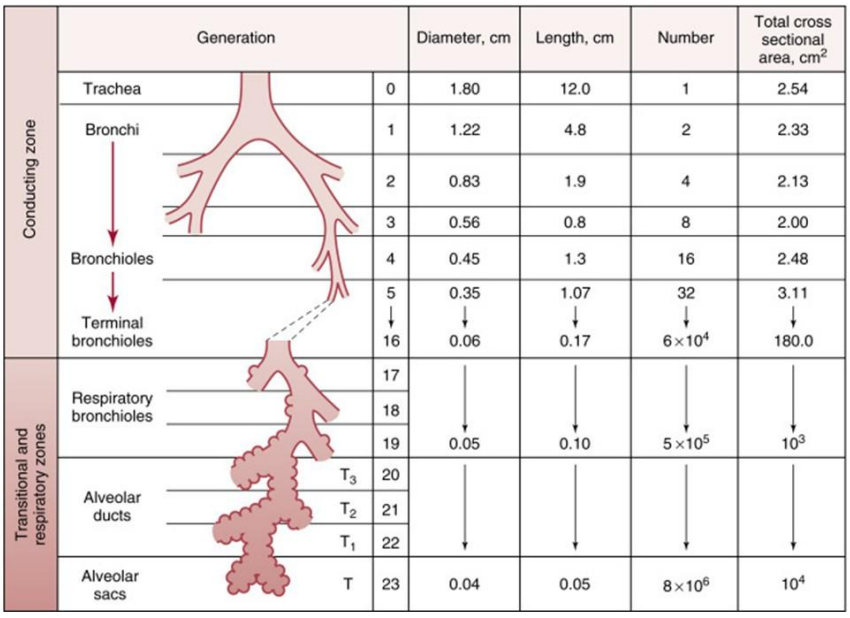

Figure 1.2 – Airway generation and approximated dimensions [c].

The respiratory zone, represented in Figure 1.3, is composed of the respiratory bronchioles, alveolar ducts, and alveoli, in which the gas exchange takes place. It is characterized by two types of cells: type 1 pneumocytes, which are the epithelial cells that form the air-blood barrier, and type 2 pneumocytes, which secrete surfactant and regenerate the epithelium [41].

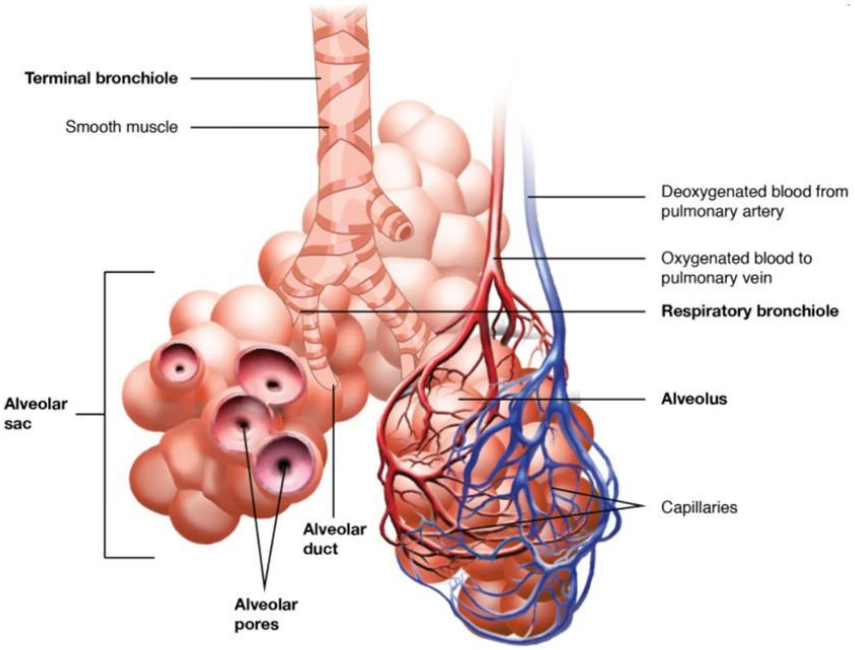

Figure 1.3 - Alveolar space anatomy [41].

Because airway geometry and structure vary along the bronchial tree, disease-related remodelling may affect airway calibre and branching patterns in a heterogeneous manner.

1.2. Pathologies of the Respiratory System

The lung and the airways can be affected by a wide range of pathological conditions, which are commonly classified into two main categories [9]:

- Obstructive diseases. These include conditions characterized by airflow limitation, primarily during expiration, resulting in air trapping and increased airway resistance. This impairment is typically caused by airway narrowing and/or loss of elastic recoil, and clinically manifests as dyspnea and prolonged expiration.
- Restrictive diseases. These conditions are characterized by reduced lung volumes and impaired lung expansion, most commonly due to increased lung stiffness (reduced compliance), but they may also arise from abnormalities of the chest wall, respiratory muscles, or neural control of breathing [d].

In particular, Hypersensitivity Pneumonitis typically presents with a restrictive pattern; however obstructive or even a mixed ventilatory defects may also be observed, depending on disease stage and airway involvement [42].

1.2.1. Hypersensitivity Pneumonitis

Hypersensitivity Pneumonitis (HP) is a heterogeneous interstitial lung disease (ILD) caused by the inhalation of specific organic antigens or low-weight molecular substances that trigger an exaggerated immune response in susceptible individuals [10]. Not the exposed subjects develop the disease, as host-related factors, including genetic susceptibility, immune regulation, and environmental exposure characteristics, play a key role in determining the response to a given antigen [11] [12].

As previously stated, the origin of the disease is related to the inhalation of specific antigens with an aerodynamic diameter of approximately 1-3 μm, which allows them to reach the distal airways and alveoli. Repeated or continuous exposure may induce a hypersensitivity response characterized by persistent epithelial injury and an aberrant immune response, ultimately leading to fibroblast activation, collagen deposition, interstitial remodelling and fibrosis [11]. Exposure may occur in domestic,

occupational, or recreational environments and is often associated with multiple antigens rather than a single identifiable source [13] [14].

HP is traditionally classified into three clinical forms according to the duration of the symptoms [15] [12]:

- Acute. Its symptoms, such as fever, chills, sweating, headache, cough, and dyspnoea appear 2-9 hours after antigen exposure, peak in 6-24 hours, and resolve within hours or days after the cessation of exposure [16].
- Subacute. The symptoms are similar but typically less severe, that persists for weeks to months and may, in some cases, progress to more severe respiratory impairment, requiring hospitalization. These changes often improve gradually after the end of the exposure [11] [16].
- Chronic. It is the final stage of the disease, which develops over months or years and is marked by progressive respiratory symptoms, fatigue, and weight loss. It is commonly associated with intermittent, prolonged, or cumulative antigen exposure and may lead to irreversible fibrotic changes that persist or progress even after the removal of the antigen [11].

1.2.2. Diagnosis

Hypersensitivity pneumonitis presents with a wide spectrum of clinical, functional, and radiological phenotypes, making its distinction from other interstitial lung diseases (ILDs), especially idiopathic pulmonary fibrosis (IPF), challenging. For this reason, diagnosis relies on a comprehensive multidisciplinary assessment, that integrates detailed exposure history, clinical evaluation, imaging, and, eventually, bronchoalveolar lavage (BAL) and transbronchial biopsy findings [17] [11] [18].

- ANTIGEN DETECTION

The identification of the causative antigen is crucial in the diagnostic process. Questionnaires allow the identification of the environments frequented by the patient, guiding targeted environmental sampling and microbiological or chemical analysis. In laboratory, an investigation to confirm the suspected antigen is performed, and afterwards, a test to confirm the causality between antigen and disease needs to be performed. For instance, a specific IgG test could verify suspicious exposures or indicate a yet undetected exposure, but there is a lack of defined values for specific IgGs, and the test is not standardized [13] [10].

- RADIOLOGY

Chest imaging represents a cornerstone of the diagnostic workflow [19]. Even though chest radiography may be normal in a significant proportion of HP patients, especially in acute HP, high-resolution computed tomography (HRCT) is the most sensitive imaging modality for evaluating suspected HP and for supporting differential diagnosis, especially when histological samples are not available [20]. HRCT allows identification of a broad range of parenchymal patterns that reflect airway, interstitial, and alveolar involvement, contributing to disease characterization and phenotypic stratification [11]. Examples of chest HRCTs are shown in Figure 1.4.

Figure 1.4 – Anatomical views of a HRCT scan [21].

- BAL

  BAL is routinely used in clinical practise for suspected HP patients, as it allows the collection of cells and soluble material from the distal airways, as represented in Figure 1.5, that are important elements for diagnosis. An increased proportion of alveolar lymphocytes should not be considered a direct indicator of HP, as lymphocytosis may also be observed in exposed but asymptomatic individuals or in patients with other ILDs [15]. Nevertheless, BAL findings can help direct the diagnosis of an ILD of unknown origin towards HP [16]. In patients with fibrotic disease, the absence of lymphocytosis does not exclude HP, while in patients with non-fibrotic disease it does [10].

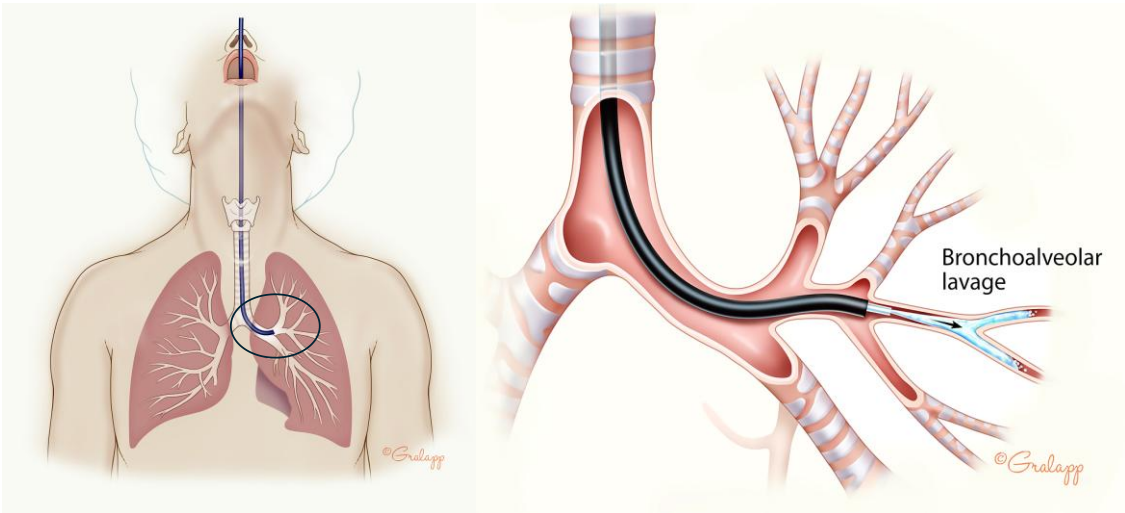

Figure 1.5 – BAL procedure [g].

- LUNG BIOPSY AND HISTOPATHOLOGY

  Before proceeding with lung biopsy, it is fundamental to examine all the other diagnostic assessments, given the invasive nature of this procedure. Lung biopsy can be performed either surgically or via transbronchial sampling. Histological findings are often complex to interpret in isolation due to the heterogeneity of HP. Specific histopathological features may support the diagnosis in non-fibrotic and fibrotic HP, while the presence of features

inconsistent with HP (or typical of other diseases) may suggest exclusion of the diagnosis [10] [13].

1.3. Computed Tomography Imaging

CT scanners consist of a motorized patient couch and a rotating gantry with a central bore, in which the couch translates during image acquisition. The gantry houses an X-ray source on one side and an array of detectors on the opposite side. During a scan, the gantry rotates around the patient, emitting X-ray beams from multiple projection angles and measuring the transmitted intensity at the detector array as depicted in Figure 1.6. These measurements allow estimation of X-ray attenuation through the tissues, from which cross-sectional images are reconstructed. In early CT systems, three-dimensional datasets were obtained by stacking multiple two-dimensional images acquired at discrete longitudinal positions of the moving couch. In modern scanners, image acquisition is performed using a helical (or spiral) CT approach, in which continuous couch translation is combined with gantry rotation and multi-row detector arrays, enabling rapid volumetric imaging [21] [22].

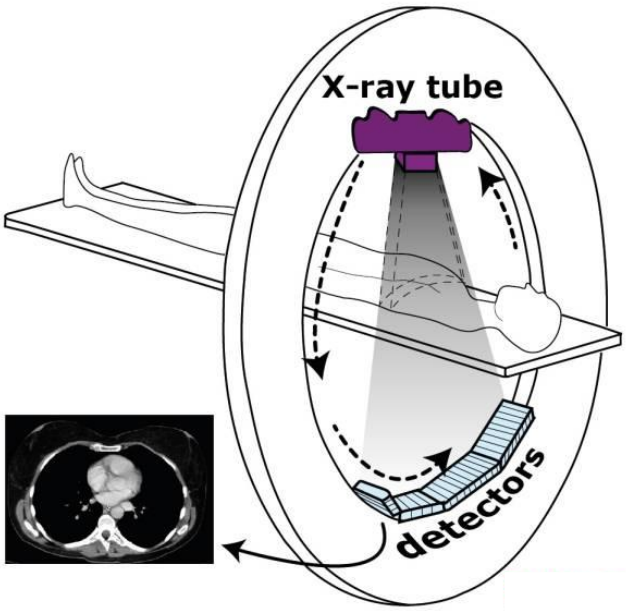

Figure 1.6 – CT acquisition modality [h].

Voxel intensities in CT images are expressed in Hounsfield units (HU), which represent the X-ray attenuation of tissues normalized to that of water. By definition, water has an attenuation value of 0 HU, while air has a value of approximately -1000 HU. Tissues with higher attenuation than water, such as bones, muscle or liver, exhibit positive HU values, whereas low-density tissues such as the lung show negative HU.

1.3.1. Chest CT scans in HP patients

1.3.1.1. Chest CT appearance of the healthy lung

Physiological chest CT scans (Figure 1.7) of the lung parenchyma and airways (excluding bones and surrounding soft tissues) are characterized by three main components, each associated with a distinct range of Hounsfield Unit (HU) values:

- Pulmonary vessels, which typically show attenuation values around +50 HU and run alongside the bronchial tree.
- Lung parenchyma, which which exhibits low attenuation values (approximately -850 HU) due to its composite structure of air-filled alveoli and soft tissue.
- Airways, which are filled with air and therefore display attenuation values close to -1000 HU.

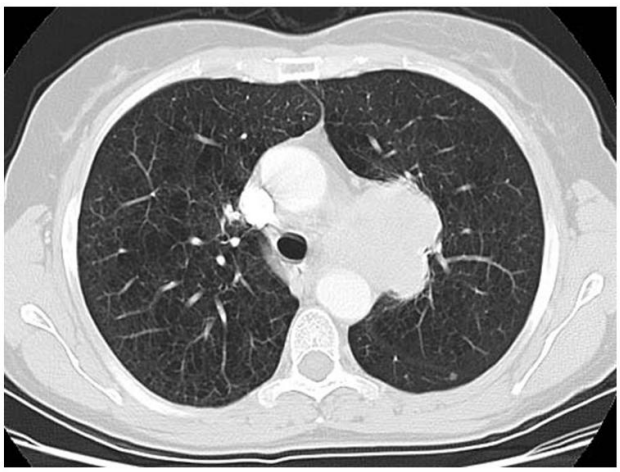

Figure 1.7 – Physiological chest CT [e].

1.3.1.2. Chest CT findings in hypersensitivity pneumonitis

In HP patients, chest CT scans reveal a variety of imaging patterns reflecting inflammatory, airway, and fibrotic involvement. The specific appearance depends on disease phase and phenotype. Acute and non-fibrotic HP patients present ground glass opacities, centrilobular micronodules, and mosaic attenuation, whereas chronic or fibrotic HP patients predominantly show fibrosis, architectural distortions, traction bronchiectasis, and, in advanced cases, honeycombing. These abnormalities may exhibit a subpleural or peribronchovascular distribution [13]. The main CT patterns observed in HP are summarized below:

- Ground-glass opacities (GGO). Areas of increased lung attenuation in which underlying vascular and bronchial structures remain visible, sometimes associated with fine textural changes but without established reticulation [23].
- Centrilobular micronodules. Small nodular opacities, often associated with GGO, reflecting bronchiolocentric inflammatory involvement of the small airways [11].
- Mosaic attenuation ("Headcheese sign"). A heterogeneous lung attenuation pattern characterized by the coexistence of areas with increased attenuation due to interstitial inflammation (as GGO), and regions with normal lung parenchyma [11].
- Fibrosis. A chronic response to repeated epithelial damage and inflammation, leading to collagen deposition, interstitial remodelling and increased lung attenuation [24] [19].
- Traction bronchiectasis. Irreversible dilatation of the airways caused by fibrotic retraction of the surrounding lung parenchyma, commonly observed in advanced interstitial lung diseases [25] [19].
- Honeycombing. The presence of clustered, thick-walled cystic air spaces, typically representing end-stage fibrotic remodeling.

To illustrate these findings, the following HRCT images provide representative examples of the previously described imaging patterns. Specifically, Figure 1.8 summarizes the patterns most commonly observed in non-fibrotic HP patients, whereas Figure 1.9shows the patterns predominantly found in fibrotic HP patients.

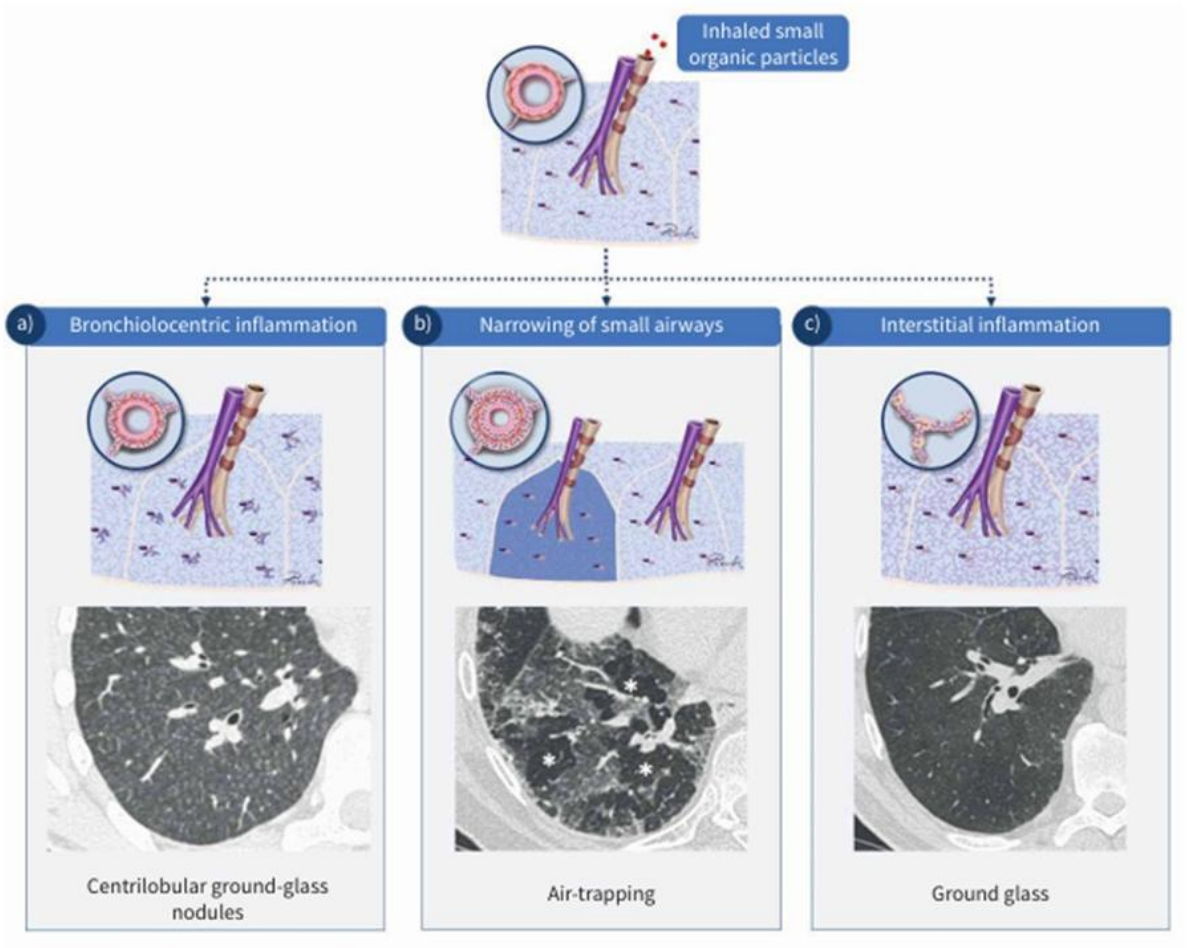

Figure 1.8 – Main patterns present especially in non-fibrotic HP patients [10].

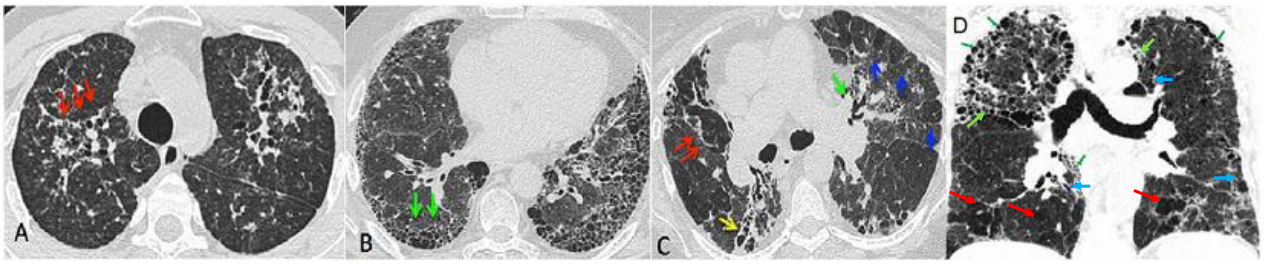

Figure 1.9 – HRCT of CHP patients [13].

(A) Patient with peribronchovascular reticulation and ground-glass opacities containing traction bronchiectasis indicated by red arrows.

(B) Patient with subpleural honeycombing, reticulation and traction bronchiectasis indicated by green arrows.

(C) Patient with peribronchovascular fibrosis indicated by green arrows, peripheral subpleural fibrosis indicated by yellow arrow, mosaicism in areas of lobular air trapping indicated by blue arrows and fibrosis near to physiological lung parenchyma that may seem of air trapping indicated by red arrows.

(D) Patient with traction bronchiectasis indicated by blue arrows, honeycombing indicated by green arrows and mosaic attenuation indicating air trapping indicated by red arrows.

1.4. Longitudinal development and assessments of CHP

CHP is characterized by a highly heterogeneous and often unpredictable course. Nevertheless, some factors have been consistently associated with disease progression and mortality. These include the impossibility of removal of the antigen, older age, male sex, smoking history, and the presence and extent of fibrotic changes on imaging, such as traction bronchiectasis and honeycombing, all of which are associated to worse survival outcome [10]. On the other hand, the presence of GGOs and mosaic attenuation are indicators of improved survival, as these patterns are generally indicative of a more inflammatory and potentially reversible disease phenotype [17].

1.4.1. Treatment of CHP

In patients with CHP, avoidance of antigen exposure should be the first thing to accomplish. When exposure avoidance alone is not sufficient, pharmacological treatment may be considered based on the predominant disease phenotype. In fibrotic CHP, immune-modulating agents and antifibrotic treatments are the main solutions, while corticosteroids are a better solution for non-fibrotic patients with higher inflammation. The use of immune-modulating agents such as azathioprine and mycophenolate, sometimes in combination with prednisone, have been shown to

improve gas exchange. However, their use remains off-label, and caution is required when combining various treatments. In patients in which disease progresses even after previously cited solutions, antifibrotic treatment may be considered, again acknowledging their off-label use and the cost-related problems [26] [13] [27].

Non-pharmacological solutions, including long-term oxygen therapy, transplant referral, and palliative care, are recommended in patients with progressive fibrosis [26].

1.4.2. Evaluation of CHP progression

A crucial aspect that needs to be addressed is the monitoring of disease progression. Currently, the current gold standard for longitudinal assessment is spirometry, with particular emphasis on forced vital capacity (FVC) [11].

1.4.2.1. Spirometry

Spirometry is an objective pulmonary function test that measures the volume and flow of air expired by the patient. It requires active patient cooperation, and its quality depends both on patient compliance and on the expertise of the operator, who must properly instruct and guide the subject throughout the maneuver. The main spirometric parameters include:

- Forced Vital Capacity (FVC): the maximum volume of air that can be exhaled after fully inhaling.
- Forced Expiratory Volume in 1 second (FEV1): the volume of air exhaled during the first second of the forced expiratory maneuver.

- FEV1/FVC ratio: the proportion of the vital capacity exhaled in the first second of the forced manoeuvre; reduced values are indicative of airway obstruction [28] [29].

Despite its widespread use, FVC presents several limitations in the context of CHP. It provides a global measure of the disease, and is relatively insensitive to regional disease progression, which may be masked by compensatory mechanisms in other lung regions and to small changes in the pathology. Additionally, spirometric measurements are relatively unsensitive to detect small airways involvement in the presence of interstitial fibrosis, as their contribution to total airway resistance is typically below 30%. As a result, pulmonary function tests may remain within normal ranges despite ongoing structural disease progression. For these reasons, high-resolution computed tomography (HRCT) has become increasingly important for disease monitoring in CHP [11].

1.4.2.2. CT analysis

HRCT pattern analysis and, in particular, automated quantitative methods, is gaining importance in the assessment of CHP. Advances in lung segmentation algorithms now allow to distinguish lung parenchyma from the airways, pulmonary vessels and surrounding tissues, enabling quantitative characterization of pathological patterns according to the abnormal variations in HU intensity. These methods provide detailed information on regional disease distribution and progression, allowing a better understanding of regional variations.

In a study performed by Choe et al. [30], CT patterns were evaluated qualitatively and semi-quantitatively by two expert radiologists, who reviewed all the CT scans and assigned scores reflecting the average extent of reticulation, honeycombing, GGOs, mosaic attenuation, consolidation, and nodules (reticulation and honeycombing were also combined to derive a total fibrosis score). They noticed that reticulation, GGO,

total fibrosis score and bronchiectasis were predictors of disease fibrotic progression and, especially in those patients, that a decrease of areas of mosaic attenuation substituted by fibrosis was frequently registered.

Aliboni et al. [2] developed an automated convolutional neural network (CNN)-based approach to objectively quantify CHP-related patterns, reducing intra-observer variability inherent to visually scored assessment. Similar results with respect to the previous study were obtained, but this method resulted in much more sensitivity in detecting disease deterioration, particularly in patients exhibiting minimal FVC decline.

1.4.3. The aim of the thesis

In line with these recent developments and with the growing emphasis on quantitative imaging biomarkers, the goal of this thesis is to develop a reproducible computational pipeline for the longitudinal assessment of airway structural variations in patients with CHP using HRCT data. The first part is devoted on the implementation of a registration algorithm to accurately align tracheobronchial trees extracted from CT volumes acquired at different time points in the same patient. Subsequently, a previously validated airway measurement algorithm is applied to derive geometrical parameters at specific measurement points along each airway branch. A correspondence search between homologous measurement points across time points is then performed, enabling direct longitudinal comparison of airway dimensions. Finally, the pipeline is evaluated on a longitudinal dataset of CHP patients, and imaging-derived measurements are analyzed in conjunction with spirometric data. Correlations and statistical analyses are performed to explore the relationship between structural airway changes and functional disease progression.

2 Materials and Methods

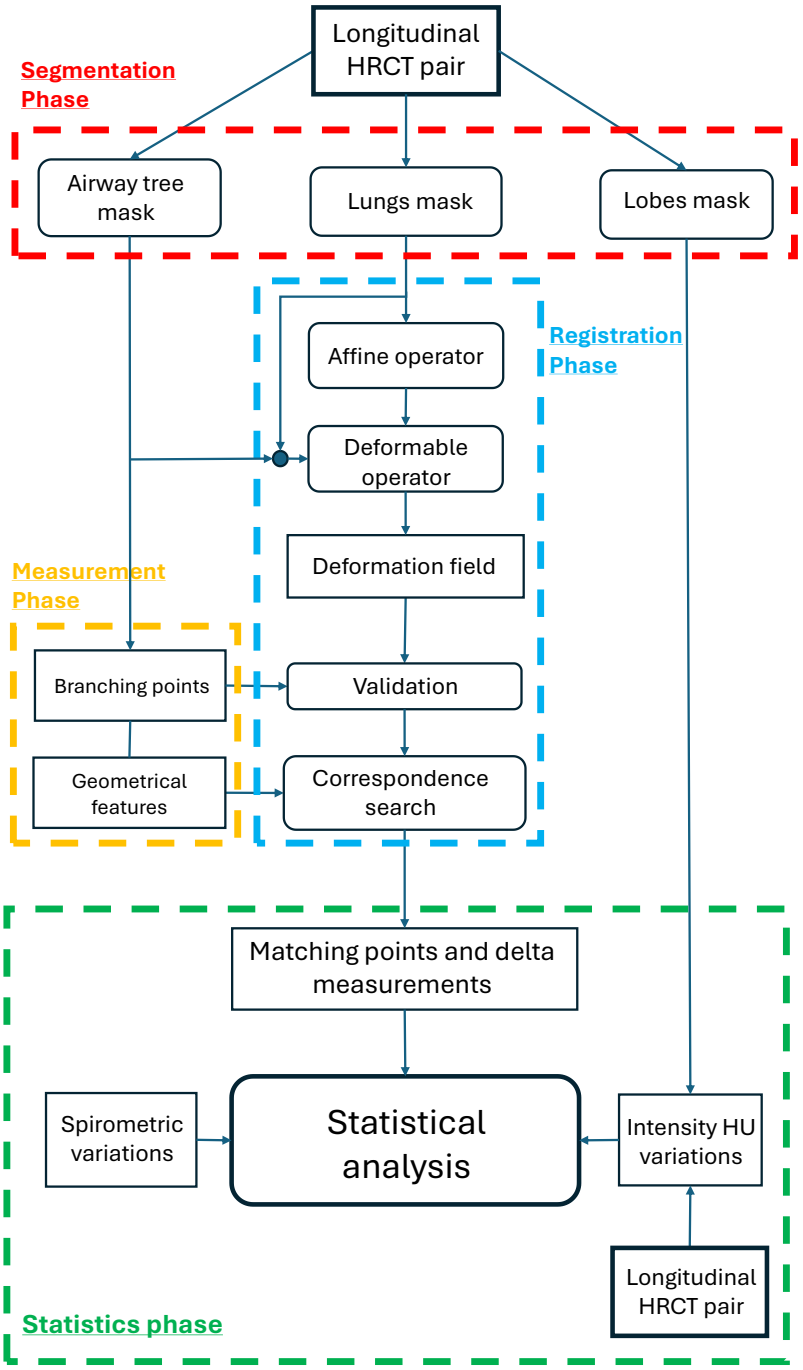

Figure 2.1 – Global workflow.

The main computational pipeline, fully developed in Python, consists of four stages schematically summarized in Figure 2.1. The first two stages are based on previously

developed frameworks that were adapted and extended for the purposes of this thesis, whereas the final two are implemented from scratch:

- Segmentation phase
- Measurement phase
- Registration phase
- Application to the CHP dataset and statistical analysis

2.1. Algorithm design and implementation

The algorithmic workflow begins with the segmentation of the input HRCT images. Subsequently, the pipeline branches in two parallel routes: the geometrical measurement module and the registration module. The final output is a list of matched airway measurement points across different time points, together with their corresponding geometrical variations. These outputs are then used for longitudinal statistical analysis.

2.1.1. Segmentation phase

The first step of the pipeline consists of extracting all anatomical structures required for subsequent processing stages from the HRCT images. The primary segmentation is the airway tree, which is necessary for geometrical measurements. In addition, whole-lung and lobar segmentations are computed, as they are required for the registration step and for statistical analyses, respectively.

2.1.1.1. Airway tree segmentation

The airway segmentation algorithm originally used in the measurement pipeline had limitations in the deep reconstruction of the tracheobronchial tree. Since accurate and distal airway measurements are crucial for this study, alternative state-of-the-art segmentation approaches were evaluated. The selection process started by reviewing the most recent public challenges focused on airways segmentation:

- "EXtraction of the Airways from CT 2009" (EXACT 09) [31],
- "Airway Tree Modelling 2022" (ATM 22) [3]
- "Airway-Informed Quantitative CT Imaging Biomarker 2023" (AIIB 23) [32].

EXACT 09 is the first benchmark challenge on the topic, but, given its age and the substantial evolution of deep learning-based approaches since its release, it was excluded [31].

ATM 22 is much more recent, including training data from both healthy subjects and Covid-19 patients. Importantly, the top-performing methods are publicly available on GitHub [3], ensuring reproducibility and facilitating implementation.

AIIB 23 instead is the most recent challenge, and its training dataset includes both healthy and fibrotic patients, making it particularly relevant for CHP. However, the winning algorithms have not been publicly released at the time of this work, preventing direct implementation[32]. For these reasons, the airway segmentation algorithm was selected from the ATM 22 challenge. The code of the top-ranked participant ("team timi") presented execution issues during testing; therefore, the implementation from the second-ranked participant ("team Yang") was adopted. Its performance metrics were comparable to those of the first-ranked method (see Figure 2.2), and it demonstrated stable execution within our computational environment.

The 1st Multi-site, Multi-domain Airway Tree Modeling (ATM'22) Challenge, MICCAI, 22 Sep 2022, Singapore.

FINAL RANKING	TEAM NAME	TD	BD	DSC	PRECISION	SCORE	INSTITUTION
1	timi	95.919	94.729	93.910	93.553	94.528	InferVision Medical Technology Co., Ltd, Beijing, China
2	Yang	94.512	91.920	94.800	94.707	93.985	Imperial College London, London, UK
3	deeptree_damo	97.853	97.129	92.819	87.928	93.932	Alibaba DAMO Academy, USA

Figure 2.2 – Airway Tree Modelling 2022 challenge top 3 results [f].

Additional segmentation algorithms, such as TotalSegmentator [4] and MEDPSeg [33], were also evaluated; but they immediately looked qualitatively worse than the "team Yang" result (Figure 2.3), which was selected as the final airway segmentation module.

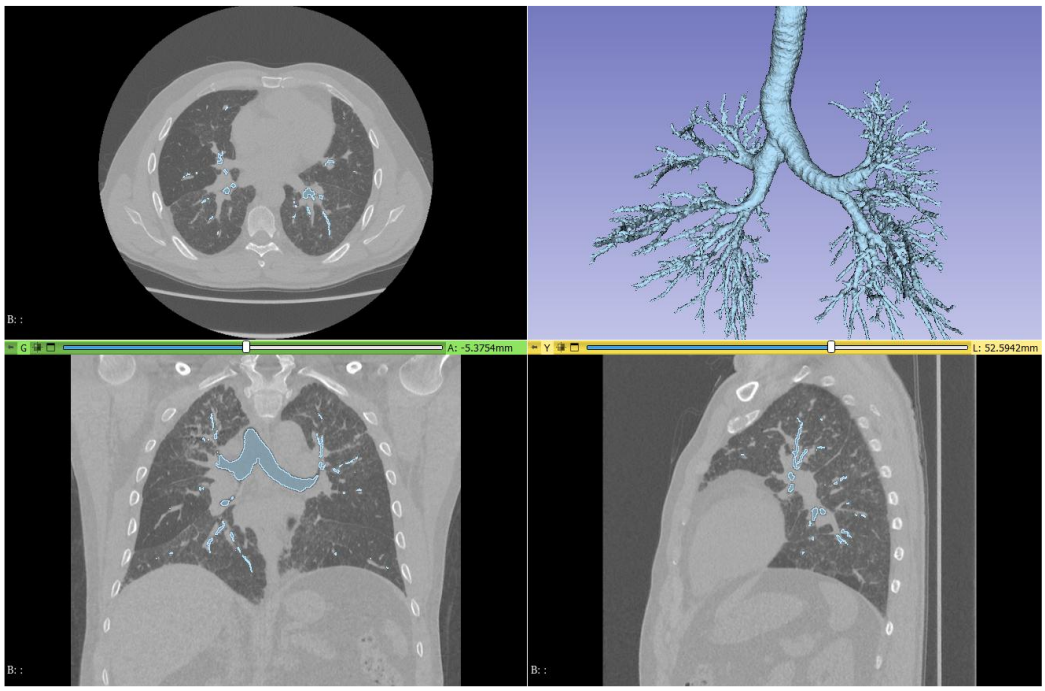

Figure 2.3 – Example of airway tree segmentation using "team Yang" algorithm [i].

2.1.1.2. Lung and lobes segmentation

Whole-lung segmentation is required to ensure accurate spatial alignment during the subsequent registration phase, while lobar segmentation allows regional statistical analyses. Due to the fact that no measurements need to be done directly on these objects, a coarse segmentation performed with TotalSegmentator is sufficient: examples of these segmentations are shown in Figure 2.4.

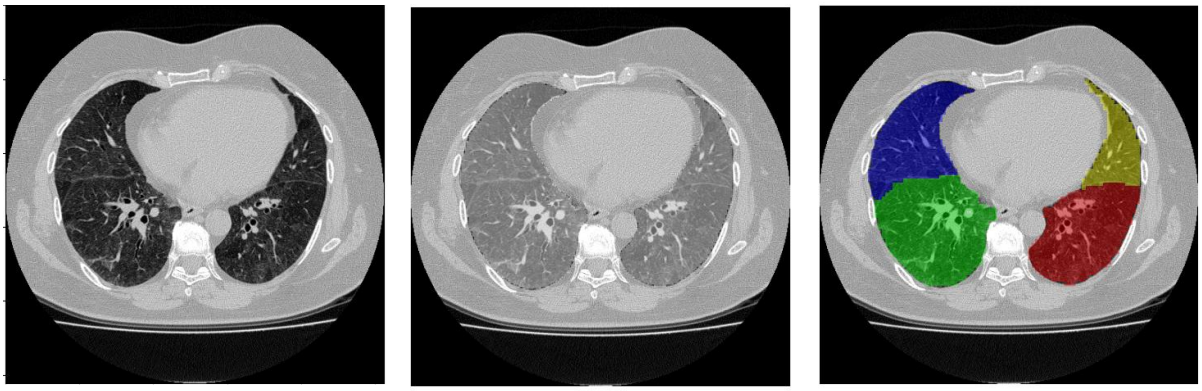

Figure 2.4 – From left to right: example of lung HRCT, lung segmentation coloured in grey superimposed to the original HRCT, lobes segmentation in different colours superimposed to the original HRCT.

2.1.2. Measurement phase

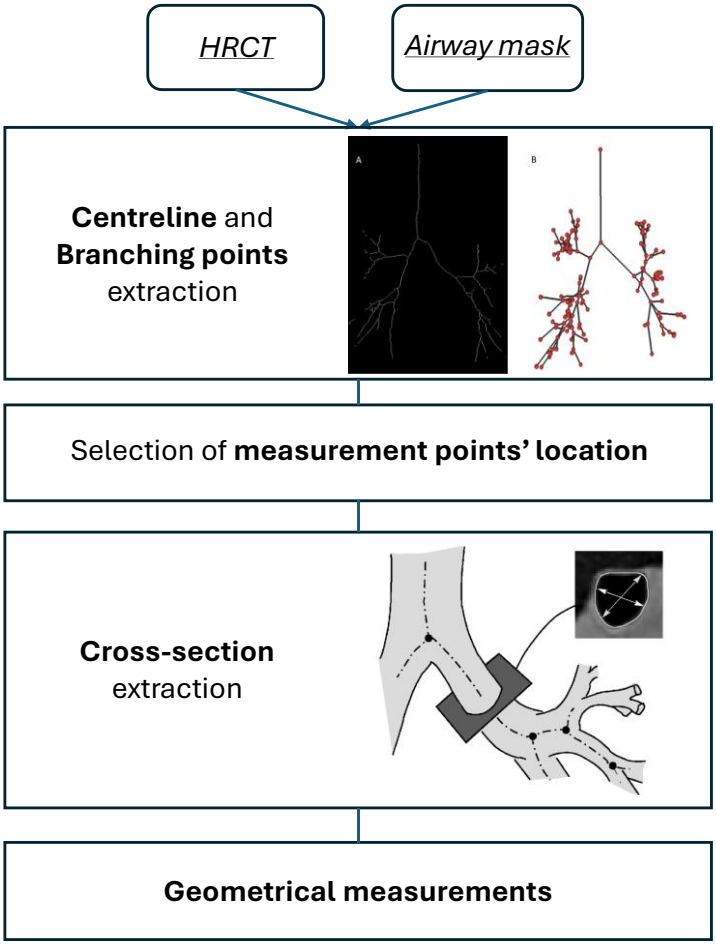

Figure 2.5 - Workflow of the measurement phase [34] [35].

Geometrical measurements on the segmented airway tree are performed using a previously validated measurement algorithm [34], that follows the schematic diagram of Figure 2.6. The algorithm first extracts the airway centreline from the binary segmentation of the tracheobronchial tree. A tree data structure is then constructed, followed by an automatic branch labelling procedure that assigns an anatomical label to each branch of the tree; however, in this work the labelling strategy was simplified to improve robustness in deeper and more complex airway trees. Specifically, anatomical labels were assigned only to trachea, main bronchi, and lobar bronchi.

Selection of measurement points. Measurement points are selected along each branch based on a normalized curvilinear coordinate ranging from 0 and 1, where 0 corresponds to the proximal end of the branch and 1 to the distal end. The original implementation allowed either single or multiple measurement points per branch by specifying one or more normalized positions. A common choice is to perform measurements at the midpoint of each branch (0.5). However, in this study a slightly more distal position (e.g., 0.6) was preferred: this choice reduces geometrical inaccuracies caused by partial branch merging near proximal bifurcations Additionally, branches shorter than 10 voxels are excluded from the measurements process and subsequent analysis.

Cross-sectional reconstruction and geometrical parameters. Once a measurement point is selected, the algorithm computes the airway cross-section at that location. This is done by:

1. Estimating the local airway direction from the centreline using two neighbouring centreline points (one proximal and one distal to the measurement point)
2. Defining the plane orthogonal to this local direction.
3. Extracting the 2D intersection between this plane and the airway segmentation mask. The resulting cross-section, combined with intensity information from the original CT volume, allows computation of several geometrical measurements, that are schematized in Figure 2.6: lumen area, edge (wall) area, total bronchial area, mean and standard deviation of bronchial wall thickness, inner major and minor axes, outer major and minor axes.

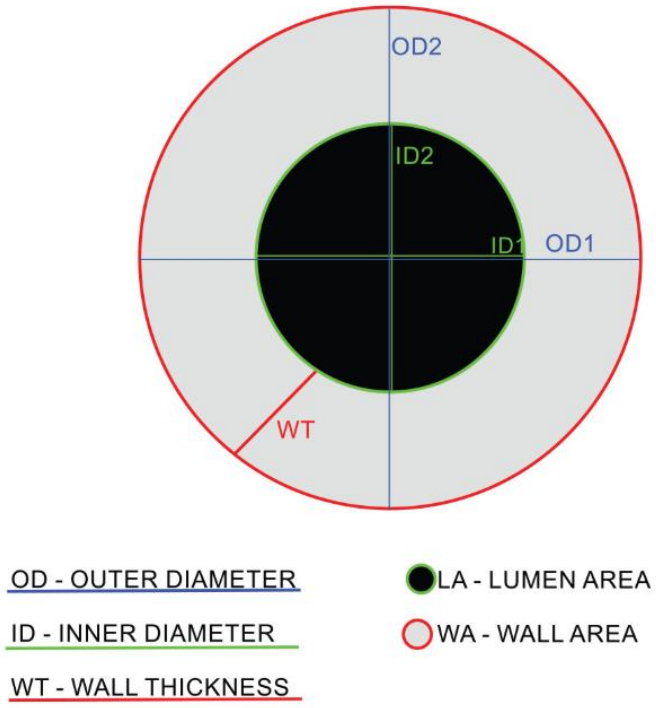

Figure 2.6 – Schematic representation of the cross section of the airway at a measurement point [36].

The position of the cutting plane is critical. If the measurement point is chosen too close to the proximal branching point (i.e. normalized position between 0.5 and 0), the orthogonal plane may intersect two partially connected daughter airways that are not yet fully separated in the segmentation mask. This leads to inaccurate geometrical estimates. The importance of proper position of the cutting plane is illustrated in Figure 2.6. This is also one of the reasons why the shortest branches are discarded, as they are mostly attached to bigger branches.

Additional outputs and validation. In addition to the measurement points' coordinates and geometrical features, the original code has been modified in order to also output branching points locations. These landmarks are later used to support validation of the registration procedure.

The measurement algorithm had been previously validated by comparing automatically extracted parameters with manual measurements evaluated in randomly selected airway cross-sections, demonstrating good agreement.

2.1.3. Registration phase

Till this moment, all the procedures, including segmentations and geometrical measurements, have been performed on single HRCT volumes acquired at a specific time point. The registration phase introduces the joint processing of two volumes from the same patients acquired at different time points. The main goal is to allow spatial superimposition and comparison of anatomical structures and their associated geometrical features, thereby allowing longitudinal analysis. In the registration framework, the earlier acquisition is defined as the fixed image, while the subsequent is the moving image, that is transformed to achieve alignment with the fixed one. The overall registration process is summarized in the schematic diagram in Figure 2.7.

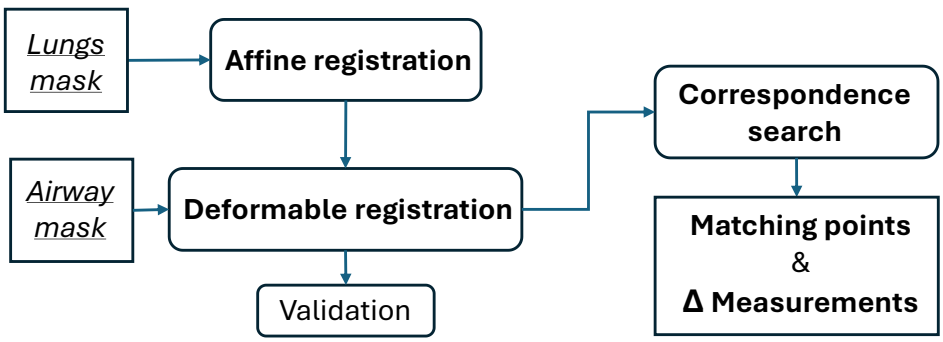

Figure 2.7 - Workflow of the registration phase.

2.1.3.1. Introduction to registration operators

Image registration methods can be broadly classified into rigid, affine, and non-rigid (deformable) transformations.

Rigid registration is the simplest model, and includes six degrees of freedom (DoF): three translations and three rotations. Although insufficient to model anatomical variations in longitudinal lung studies, rigid registration provides a crucial initialization step for subsequent affine or non-rigid transformations [37].

Affine registration extends the rigid model to 12 DoF, by including scaling and shearing components. While still globally linear, affine transformations can partially account for global anatomical changes such as differences in lung inflation. In most applications, affine registration is used as a pre-alignment step prior to non-rigid methods [37].

Non-rigid (deformable) registration is designed to capture local anatomical changes that cannot be explained by global linear transformations. These methods balance asimilarity metric between images while enforcing regularization constraints to ensure smooth, physically plausible deformations and to avoid overfitting [38].

Two major deformable strategies were considered:

- Free-form deformation (FFD) based on B-splines, where the deformation field is controlled by a sparse grid of control points and interpolated using B-spline basis functions. This approach provides a good compromise between flexibility and computational efficiency and is commonly implemented in a multi-resolution (coarse-to-fine) scheme, with explicit smoothness constraints on the deformation to promote realistic warps [39].
- Demons-based methods, which iteratively compute a dense displacement field inspired by optical flow principles. To address limitations of the original formulation (e.g. lack of guaranteed invertibility and topology preservation), the diffeomorphic demons variant was adopted. This formulation ensures smooth and invertible transformations while retaining computational efficiency, making it particularly suitable when anatomically meaningful, one-to-one mappings are required [40].

2.1.3.2. Affine registration strategy

Before proceeding with deformable registration, an adequate pre-alignment is essential to estimate the affine transformation. Several strategies were investigated to estimate the affine registration.

A first approach consisted of registering the complete airway tree segmentations. However, the high structural complexity and variability of peripheral branches resulted in unstable and unreliable affine transformation.

Alternative strategies included:

- Registration of a pruned airway tree including only trachea, and right and left bronchus.
- Registration of a pruned airway tree including also the five lobar bronchi.

Although these strategies improved qualitative alignment compared to the full-tree registration, quantitative evaluation at this stage was not reliable due to persistent mismatch in peripheral branches. The final and most effective strategy focused on performing affine registration on the whole-lung segmentations extracted from HRCT images. This global anatomical alignment yielded more robust and consistent results, as shown in Figure 2.8.

By aligning entire lung volumes rather than airway trees alone, the subsequent deformable field describes the real local deformation experienced by each piece of airways starting from the same position with respect to the lungs. This approach ultimately proved to be the most stable and reproducible solution.

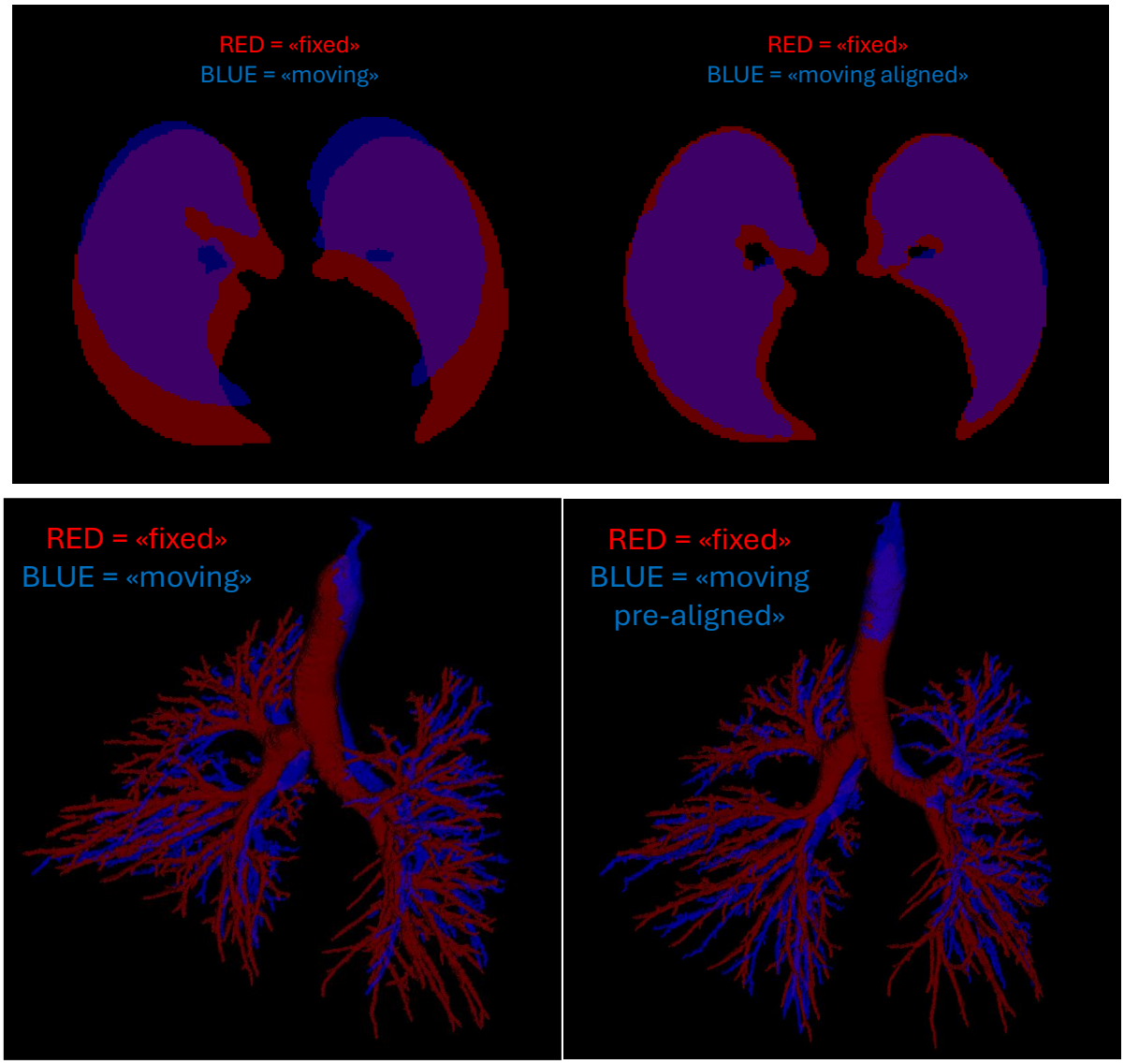

Figure 2.8 – From top to bottom: affine alignment of two lungs masks; visualization of fixed and moving airway mask before and after the application of the estimated affine operator.

2.1.3.3. Deformable registration

Deformable registration is performed after affine pre-alignment. Different deformable strategies were initially tested while keeping the affine initialization fixed. Once the optimal deformable model was identified, different affine initializations were compared using the same deformable framework. The goal is to obtain a deformation field that ensures a level of airway superimposition comparable to that shown in

Figure 2.9. The estimated field instead can be visualized to identify regions experiencing larger deformations as shown in Figure 2.10.

Two main strategies were evaluated:

1. Registration of airway tree segmentations. Both B-Spline FFD and diffeomorphic demons were tested using a multiscale scheme (shrink factor: 8-4-2-1; progressively decreasing smoothing; 200 iterations at coarse level and 100 at finer levels). However, direct registration of airway segmentations did not yield satisfactory results.
2. An alternative strategy involved the same registration pipeline directly on HRCT volumes. Three variants were tested: (1) raw HRCT images, (2) airway-enhanced images, (3) airway-saturated images. The airway-saturated configuration provided the most robust results.

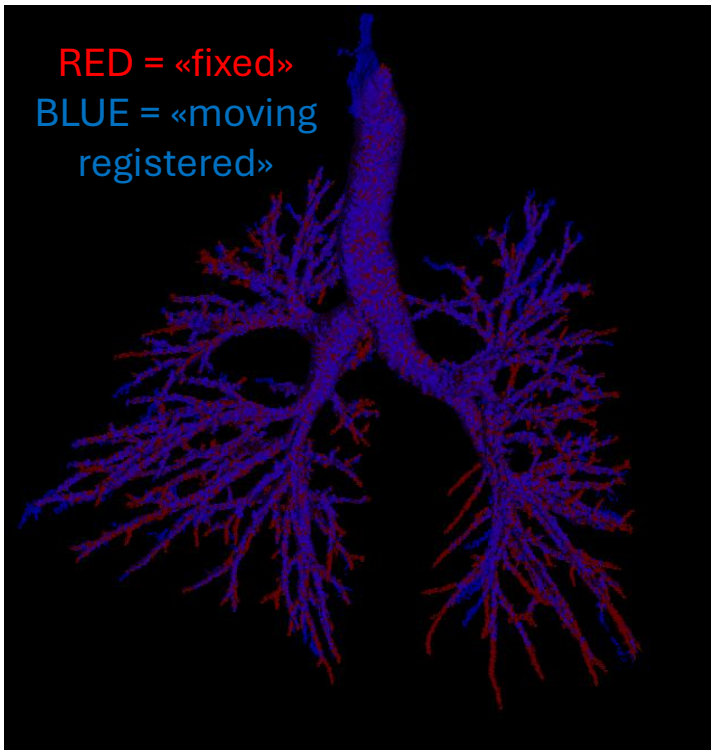

Figure 2.9 – Moving and fixed airway segmentations after deformable registration.

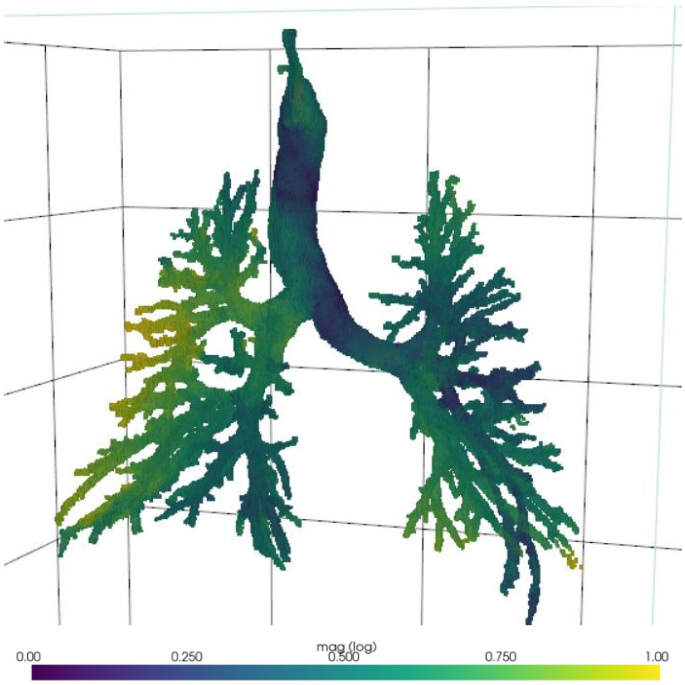

Figure 2.10 – Moving airway segmentation colored according to the deformation field applied: logarithmic scale has been applied to better enhance also small deformations.

2.1.3.4. Evaluation and validation

To objectively compare registration strategies, a quantitative evaluation was implemented by calculating the target registration error (TRE) on the airway branching points, that are extracted from the two airway trees. The affine and deformable transformations are applied to bifurcation points of the moving volume. Correspondence is established by nearest-neighbor matching, and the Euclidean distance between matched pairs is computed. Mean, median, and maximum TRE values, are calculated to assess alignment accuracy.

2.1.3.5. Correspondence search

With an analogue method, correspondence between measurement points extracted during the measurement phase is established. The affine and deformable registrations are applied to the moving measurements points. Correspondence is again determined

via nearest-neighbor search. To mitigate mismatches due to structural differences between trees, only point pairs within a predefined distance threshold are retained.

For each matched pair, geometrical measurements are retrieved and differences are computed both in absolute terms (mm) and as relative percentage variation. The final output of the computational pipeline is therefore a structured list of longitudinal geometrical variations across all matched airway segments.

2.1.4. Lung intensity analysis

In addition to airway geometrical analysis, whole-lung and lobar segmentations are used to compute global and regional lung density metrics. Mean Hounsfield Unit (HU) values are calculated at both global and lobar levels. Increased mean lung density is typically associated with fibrotic progression or other pathological processes leading to reduced aeration, as can be seen in Figure 2.11.

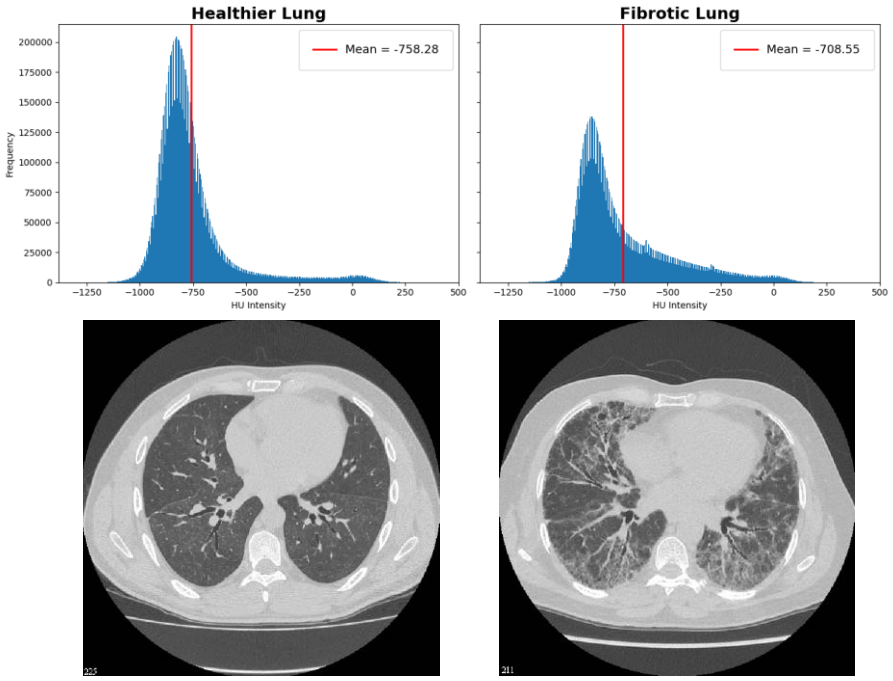

Figure 2.11 - Histogram comparison between the lungs of a patient before and after fibrotic progression. The healthier lung has a sharper peak with respect to the fibrotic one that has a broader intensity distribution. In this example it is also possible to observe a mean HU intensity higher by 50 HU in the fibrotic lung.

Each measurement point is associated with its corresponding lung lobe using lobar segmentation masks. This enables computation of regional (lobar) mean geometrical variations for each patient, allowing subsequent statistical analyses to spatially investigate disease progression.

2.2. Comparative analysis on a CHP dataset

This part is the core of this thesis, as the application of the registration tool on a longitudinal dataset of CHP patients allows to retrieve a great amount of data that may emphasize trends and typical remodelling behaviours. The following study is explorative, single-centre and retrospective.

2.2.1. Dataset

The dataset is composed by noncontrast-enhanced, inspiratory chest CT performed for a cohort of 27 fibrotic HP patients. Patients were scanned on a Brilliance 16P scanner (Philips Medical Systems, Andover, MA), from lung apices to bases, at full inspiration, after standardized breathing instructions, using a weight-based CT technique for dose minimization. The imaging parameters were: tube voltage around 120-140 kVp, tube current set to 30 mAs, pixel matrix of dimension 512x512, slice thickness of 0.8-1 mm and two types of reconstruction filter (body and lung).

Additionally, each patient performed spirometric evaluations within a time window closer to each acquisition date. The parameters measured were: FVC, FEV1, FEV1/FVC, TLC, RV, and DLCO, all expressed both in litres and in percentages.

2.2.2. Statistical analysis

As previously stated, the gold standard to evaluate disease progression in CHP patients is FVC. For this reason, patients were stratified into three groups according to longitudinal FVC variation:

- Stable : $|\Delta FVC| < 5\%$
- Worsening : $\Delta FVC < -5\%$
- Improving : $\Delta FVC > +5\%$

The variation (Δ) is defined as:

Δ = valueT2 - valueT1

where T1 and T2 represent the first and the second time points, respectively. The same definition applies consistently to FVC, geometrical airway measurements, and HU-based intensity metrics.

To ensure comparability across different airway generations and baseline sizes, geometrical variations are expressed as relative percentage changes with respect to the baseline value rather than as absolute differences (mm).

For each group of patients, both a global and a local analyses are performed:

- Global analysis. It involves patient-level aggregated parameters, including total ΔFVC, total lung ΔHU (mean intensity variation), and mean percentage values of Δ of geometrical airway features. Descriptive statistics are reported for each patient group. Data distribution is visualized using box plots. To assess differences between groups, parametric statistical tests (t-tests) are performed when normality assumptions are met. Statistical significance is evaluated using a predefined alpha threshold ($\alpha = 0.05$).
- Local (lobar) analysis. It requires lobar segmentation to evaluate spatial heterogeneity of structural changes. For each lobe, the following parameters are computed: mean lobar ΔHU and mean lobar percentage values of Δ of

geometrical airway features. Within each patient and lobe, relationships between imaging-derived parameters are explored to identify possible associations between regional densitometric changes and airway remodeling.

3 Results

3.1. Reduction of the dataset

After reviewing the complete dataset, a substantial number of subjects have been discarded due to predefined quality criteria. Exclusion criteria included:

- Images and/or spirometric measurements at one of the time points were missing.
- Images and corresponding spirometric measurements were too distant from each other (>1 month).
- Patient positioning was not supine but prone.
- The difference in in-plane spatial resolution between paired scans was too high ($\Delta > 0.1$ mm).
- The slice thickness was too high (images with $\Delta z = 0.8$ mm were kept, $\Delta z = 1$ mm excluded).

For these reasons, the initial dataset of 27 patients was reduced to 9 eligible subjects. For each patient, one or more images pairs were available; 2 patients had 1 image pair, 3 patients had 2 image pairs, 2 patients had 3 image pairs and 2 patients had 4 image pairs. All image pair was classified according to ΔFVC into stable, worsening, or improving groups. The distribution of ΔFVC across groups is shown in Figure 3.1.

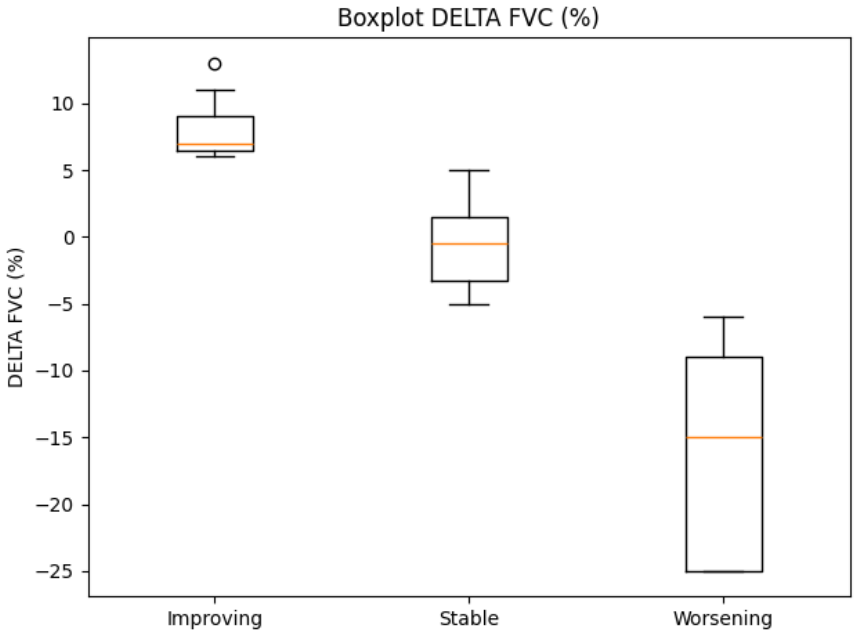

Figure 3.1 – Boxplot of ΔFVC values across the three patient groups.

3.2. SEGMENTATION PHASE: qualitative evaluation

The segmentation phase produced three main anatomical objects: whole-lung masks, lobar masks and airway tree segmentations. As previously stated, lung and lobe masks were used primarly for registration and regional stratification (and not for direct geometrical measurement), thus a single segmentation framework (TotalSegmentator) was evaluated. Visual inspection confirmed adequate segmentation quality (Figure 3.2).

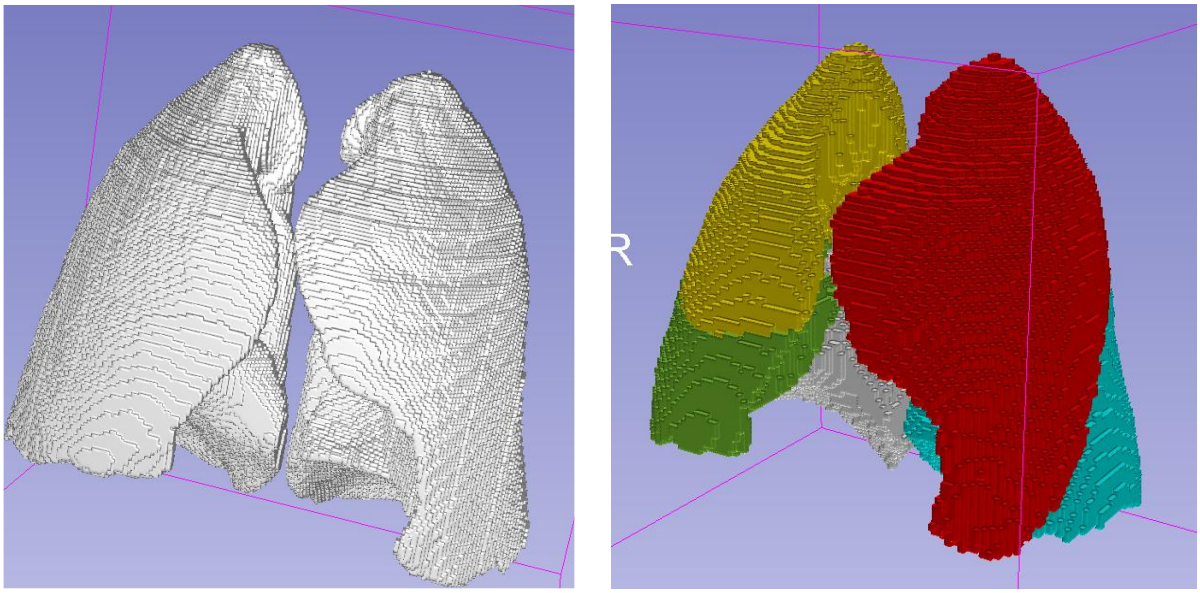

Figure 3.2 – Examples of lung (left) and lobar (right) segmentations obtained with TotalSegmentator [4].

The airway tree segmentation instead was the critical component of this phase, as geometrical measurements depend directly on segmentation accuracy. Three algorithms were qualitatively evaluated: Total Segmentator, MEDPSeg, and ATM'22 (team "Yang") pretrained model. TotalSegmentator and MEDPSeg produced acceptable results of proximal generations, but afterwards exhibited substantial limitations distally. Specifically, segmentations had a lot of small, disconnected islands and loss of distal airway continuity, as illustrated in Figure 3.3. Post processing strategies involving morphological closing or smoothing were applied (Figure 3.4), but altered airway geometry, which is crucial in this framework.

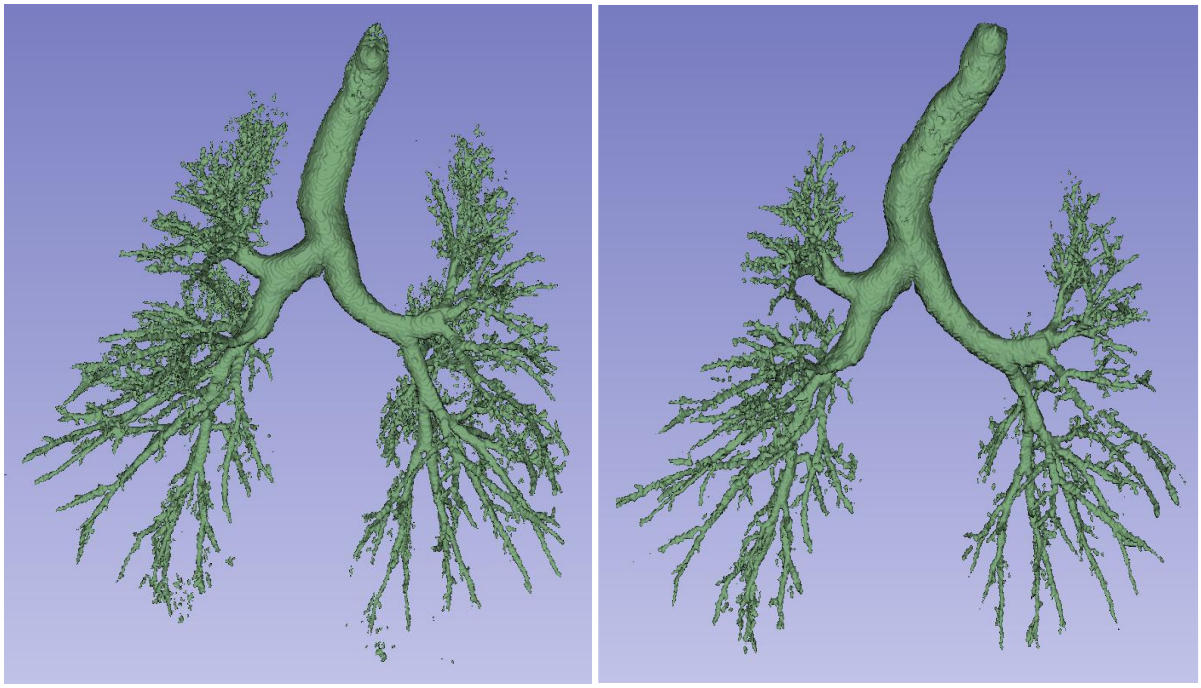

Figure 3.3 – Examples of airay segmentations obtained from the same HRCT using TotalSegmentator (left, [4]) and MEDPSeg (right, [33]).

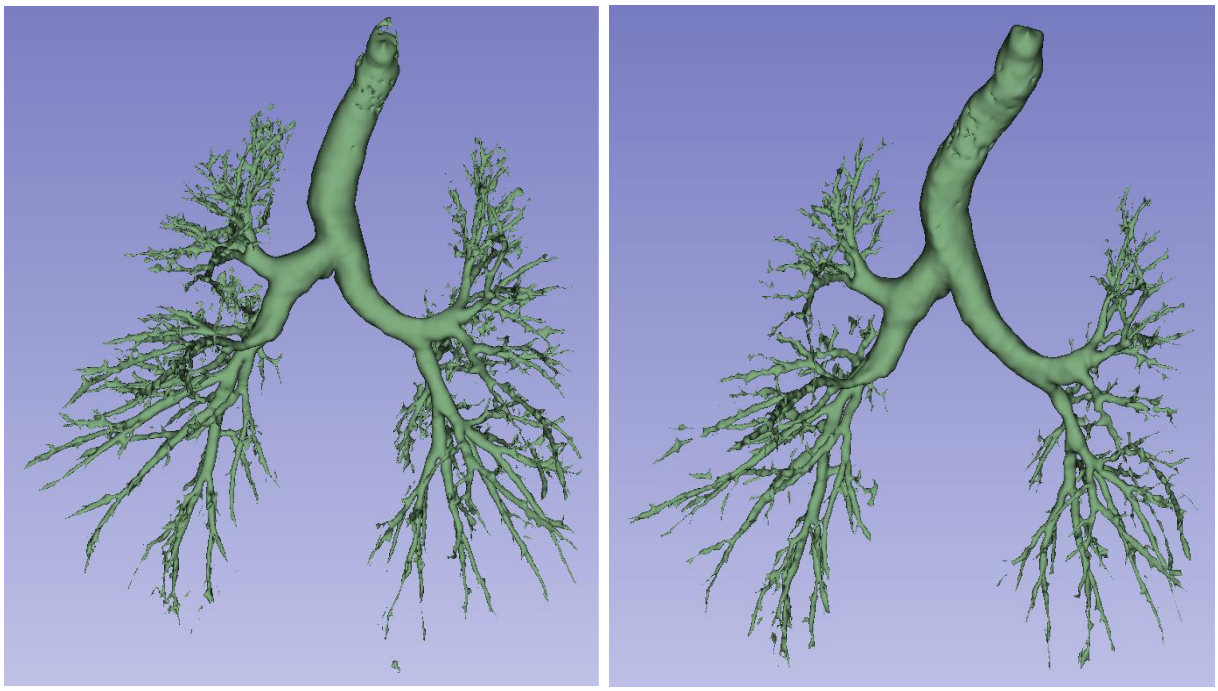

Figure 3.4 – Post-processed airway segmentations of the previous figure: Visual continuity improved, but geometrical dimensions are altered.

The most reliable results were obtained with the pretrained model from the second-ranked team in the Airway Tree Modelling 2022 challenge (team "Yang"). This model retrieved the whole airway tree without disconnection or erroneous thinning (Figure 3.5). Across the dataset, segmentation depth reached the 8th and the 9th airway generation.

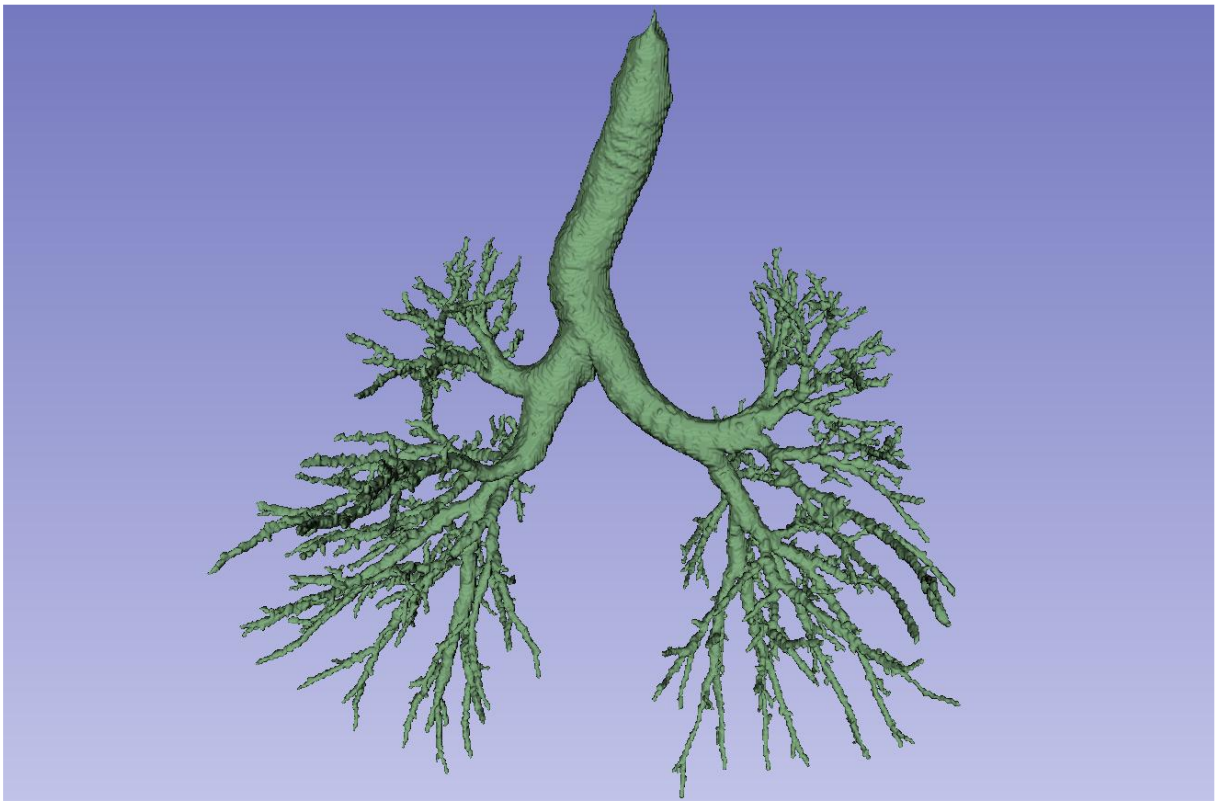

Figure 3.5 – Airway segmentation obtained using the ATM'22 team "Yang" model [i].

3.3. REGISTRATION PHASE: Validation process

The validation process required the estimated deformation field and extracted airway branching points. Validation was performed by applying the affine and deformable transformations to branching points of the moving image and computing the Euclidean distance to corresponding points in the fixed image (Target Registration Error, TRE).

A challenge arises when validating longitudinal airway registration: the number and lengths of the segmented branches at different time point often differ. Consequently, not all branching points in the fixed segmentation have anatomical correspondences in the moving segmentation, and vice versa. A solution to this problem, for validation purposes only, was adopted: the fixed image was reconstructed using a standard "lung" kernel, while the moving image was reconstructed using a "body" kernel. The coarser reconstruction leads to an airway segmentation that goes less in depth, increasing the likelihood that all moving branching points are included within the fixed set. In this configuration: each moving branching point is matched to its nearest fixed neighbour, some fixed points are not matched, which is acceptable.

This strategy avoids arbitrary exclusion of branching points based only on distance threshold, which could alter the TRE results by confusing true anatomical differences with registration errors.

Qualitative visualization. Figure 3.6-3.8 illustrate the validation setup: Figure 3.6 and Figure 3.7 show fixed and moving airway segmentation with branching points, respectively, while Figure 3.8 shows superimposed segmentations and matched branching points, with a detailed view to emphasize the validation matching process.

Figure 3.6 – Image representing the fixed airway segmentation of longitudinal pair of HRCTs (in red) with the branching points (in yellow): for simplicity of visualization, not all the existing points are shown but only the ones that will be coupled.

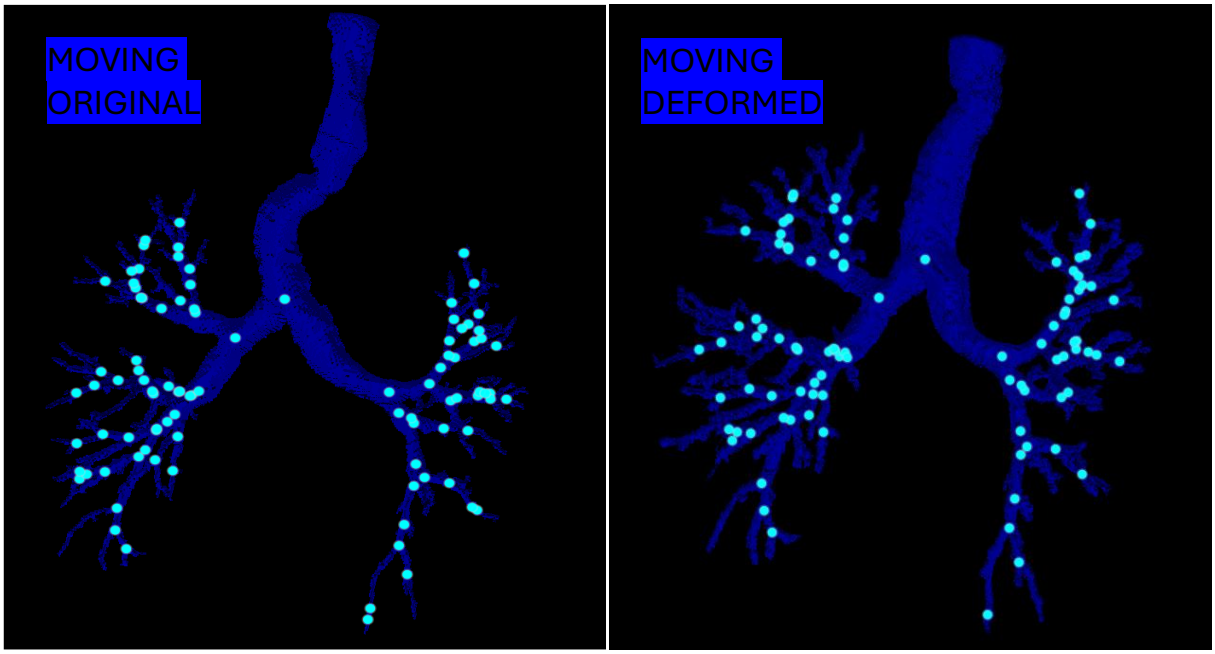

Figure 3.7 – Images representing the moving airway segmentation of a longitudinal pair of HRCTs (in blue) with all the existing branching points (in cyan): on the left the original segmentation in shown, on the right the deformed one is showed.

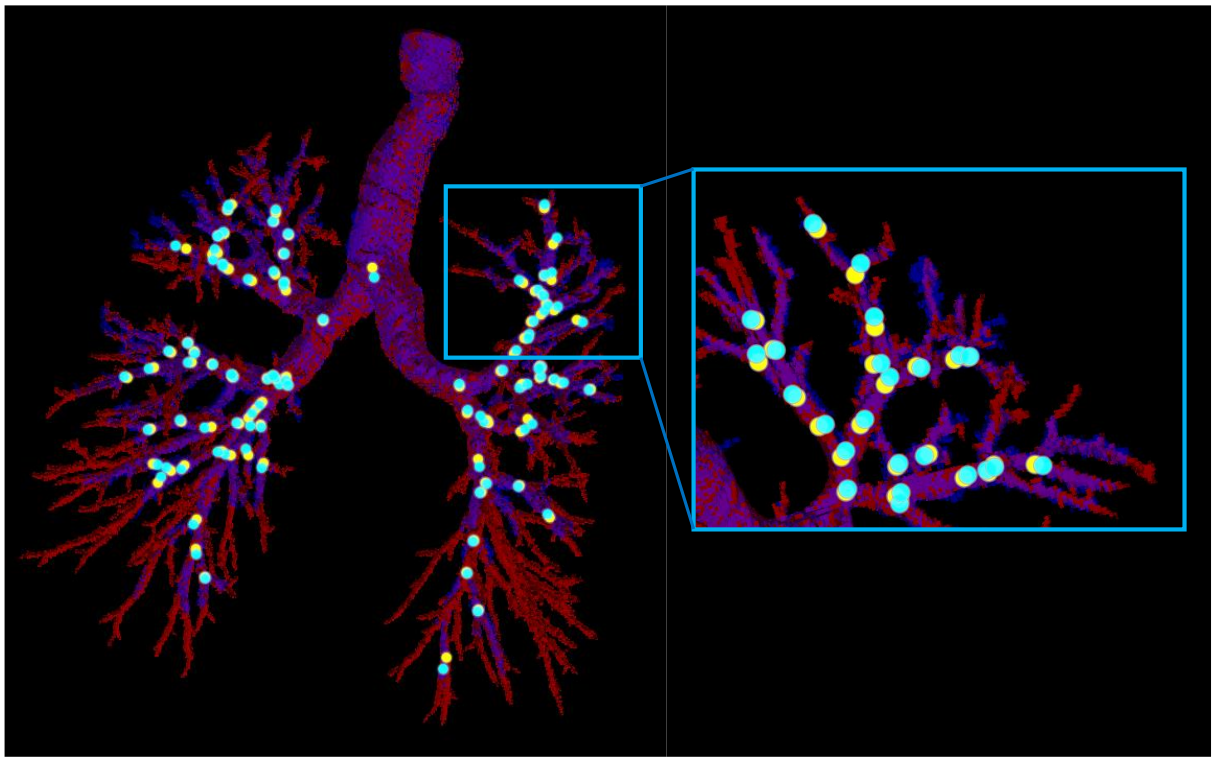

Figure 3.8 – Fixed and moving deformed airway segmentations superimposed and their corresponding branching points: the visualization of 3D objects on a 2D image is trivial, as far and close object appear on the same level, so a detail of this superimposition from a different viewing angle is better shown in the light blue box on the right.

Across the tested registration strategies, the initial TRE before any transformation was 150.72 mm (median), with an interquartile range (IQR) of 138.55-168.23 mm. After the initial affine alignment, TRE decreased to 6.76 mm (median), with an IQR of 5.31-8.45 mm. Finally, after optimization of affine and deformable parameters, TRE reached 1.50 mm (median), with an IQR of 0.96-2.07 mm. Considering a slice thickness of 0.8 mm, the final TRE corresponds to approximately 2 voxels along the z-axis, which is considered acceptable for longitudinal analysis.

Correspondence between measurement points was determined using a distance threshold. Points pairs separated by more than 5 mm were excluded from the analysis and considered as non-corresponding anatomical points due to structural differences between airway trees.

3.4. STATISTICS PHASE: analysis on the dataset

As introduced previously, the overall dataset was stratified into three groups (Improving, Stable, and Worsening) according to ΔFVC. All subsequent analysis were performed separately for each group and then compared to identify potential trends and differences.

Global lung intensity variation. Global intensity variations were first evaluated. A clear separation between the three groups emerged in terms of mean global ΔHU (Figure 3.9):

- The Improving group had mainly negative ΔHU values (reduction of the mean lung density).
- The Stable group had small variations centered around zero.
- The Worsening group had only positive ΔHU values (increase in mean lung density).

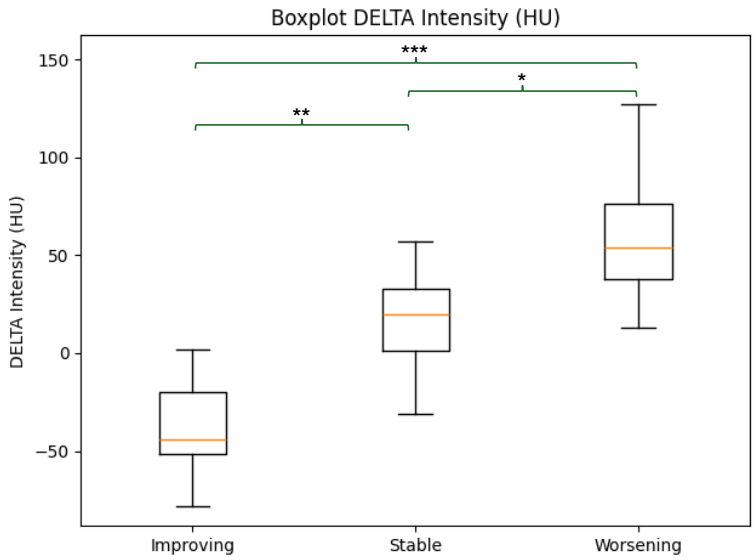

Figure 3.9 – Boxplot of mean global ΔHU in the three FVC-based groups. * $p \leq 0.05$, ** $p \leq 0.01$, *** $p \leq 0.001$.

These findings are consistent with the expected physiological relationship between functional improvement (ΔFVC > 0) and decreased lung density, and vice versa. The relationship between ΔFVC and ΔHU is illustrated in Figure 3.10.

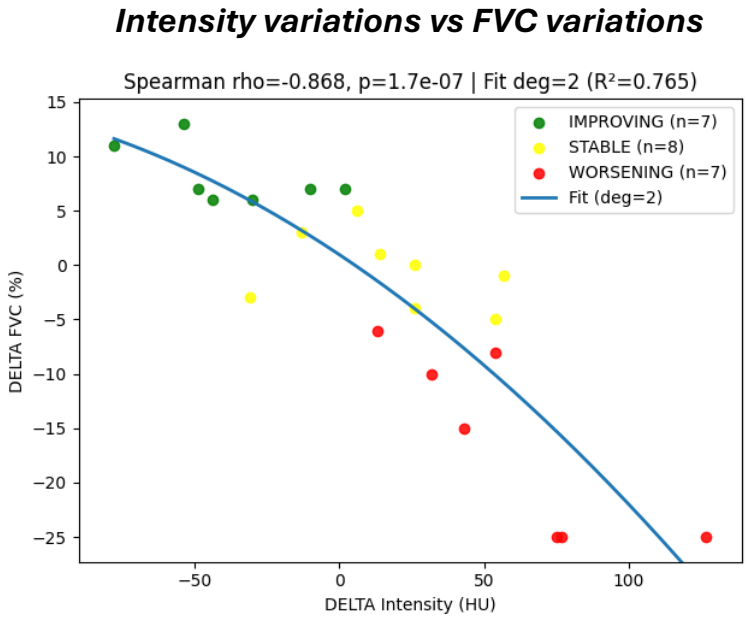

Figure 3.10 – Relationship between ΔFVC and global ΔHU.

To visually support the FVC-based classification, representative longitudinal HRCT pairs are shown in Figure 3.11.

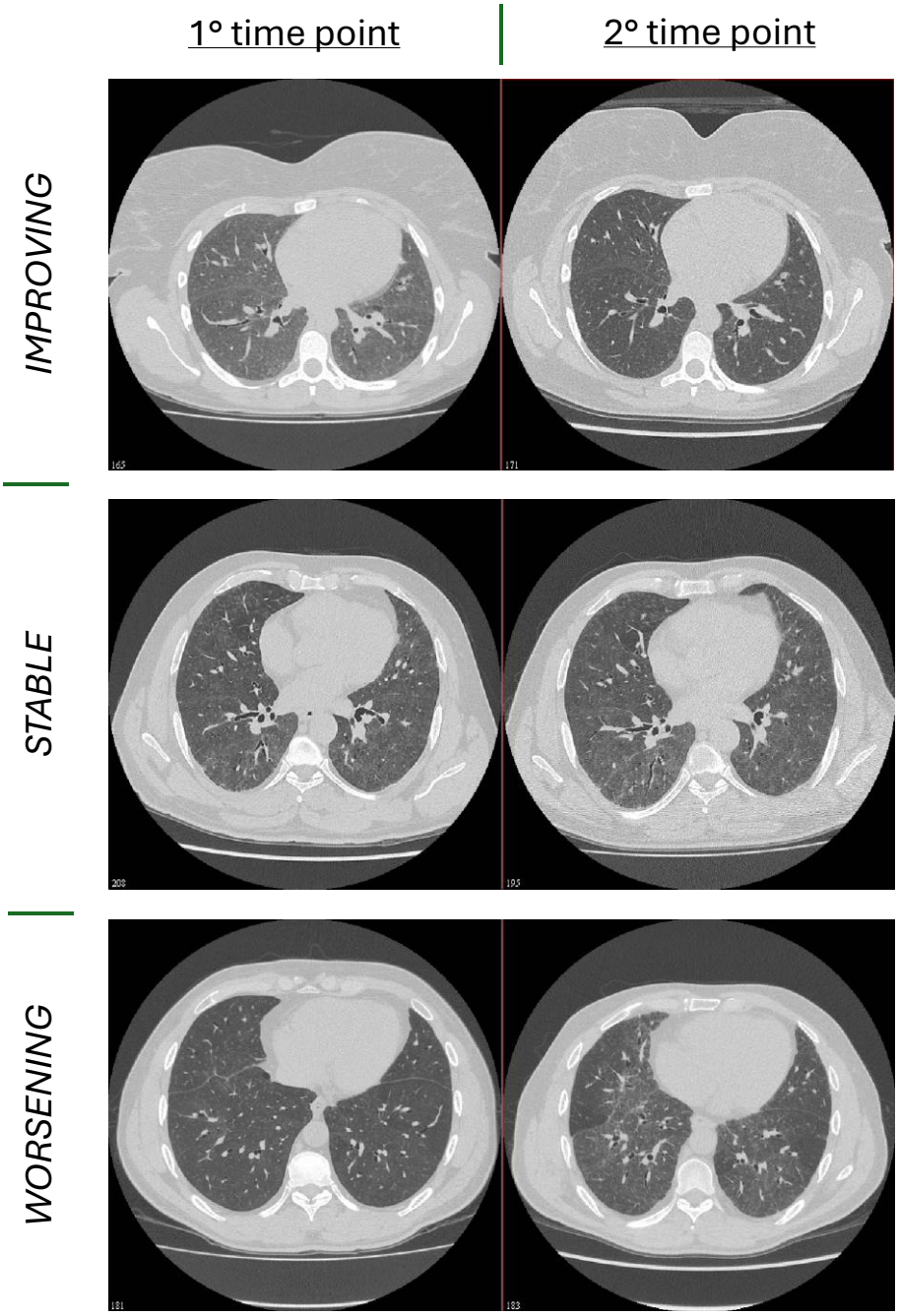

Figure 3.11 – Examples of patients with improving, stable and worsening FVC.

Global airway geometrical variations were then evaluated. Wall thickness mean and std dev were excluded from the analysis due to lack of robustness. The remaining parameters are summarized in Table 3.1. Overall:

- The Improving group showed mainly positive percentage variations across most geometrical measure (increase in total, lumen, and edge areas).
- The Stable group exhibited variations cantered around small values close to zero.
- The Worsening groups showed variations also centered near zero, with slightly more negative values in some parameters.

Despite these observable trends, none of the global geometrical parameters reached statistical significance between groups (all p-values > 0.05).

	IMPROVING (median [IQR])	**STABLE** (median [IQR])	**WORSENING** (median [IQR])	**p-value**
Δ Total area (%)	17.45 [27.21]	4.13 [6.47]	3.03 [13.94]	0.30
Δ Edge area (%)	11.49 [16.44]	1.34 [7.93]	0.00 [10.10]	0.31
Δ Lumen area (%)	24.66 [34.64]	8.05 [9.22]	5.56 [14.84]	0.24
Δ Inner Major Axis (%)	8.41 [16.20]	2.88 [4.77]	2.70 [4.26]	0.34
Δ Inner Minor Axis (%)	11.26 [13.86]	1.78 [4.41]	1.82 [6.46]	0.24
Δ Outer Major Axis (%)	7.23 [11.78]	1.83 [5.43]	2.05 [4.11]	0.33
Δ Outer Minor Axis (%)	7.92 [10.89]	1.04 [3.42]	1.50 [5.34]	0.31

Table 3.1 - Median and inter quartile range values for different measurements' variations in the three different groups.

Regional analysis. Given the limited discriminative power of global geometrical metrics, a regional (lobar) analysis was performed to explore potential spatial associations between local density changes and airway remodeling.

For each lobe of each patient, the relationship between ΔHU and percentage Δ of airway geometrical parameters was evaluated. The relationship between lobar ΔHU and areas variations for each group are shown in Figure 3.12.

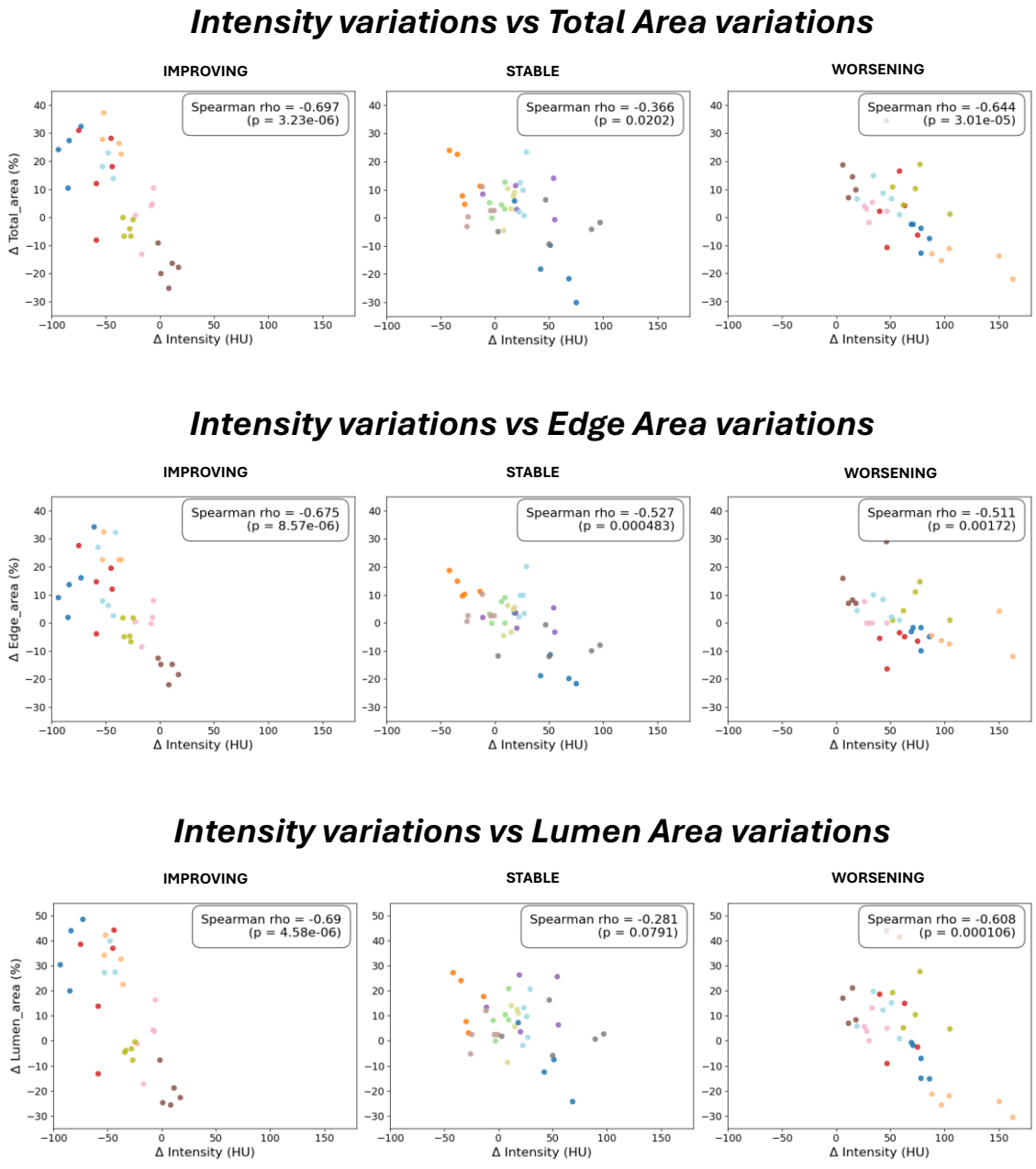

Figure 3.12 – Plots representing the relationship between the variations of areas measurements and the variations of HU in the three different groups (Spearman coefficients are reported with their p-value): the dots with the same color are representing the different lobes of the same patient.

Key observations:

- In the Improving group a steep, and significant inverse relationship was observed: decreasing density was associated with increasing airway areas.
- The Stable group exhibited a weak or absent monotonic association, especially considering the lumen area.
- The Worsening group showed a better inverse relationship considering total and lumen area in particular, even though with a different steepness with respect to the first group.

A similar analysis was performed for principal axis dimensions (Figure 3.13). Only minor axis results are shown, as they demonstrated stronger and more consistent correlations than major axis measurements.

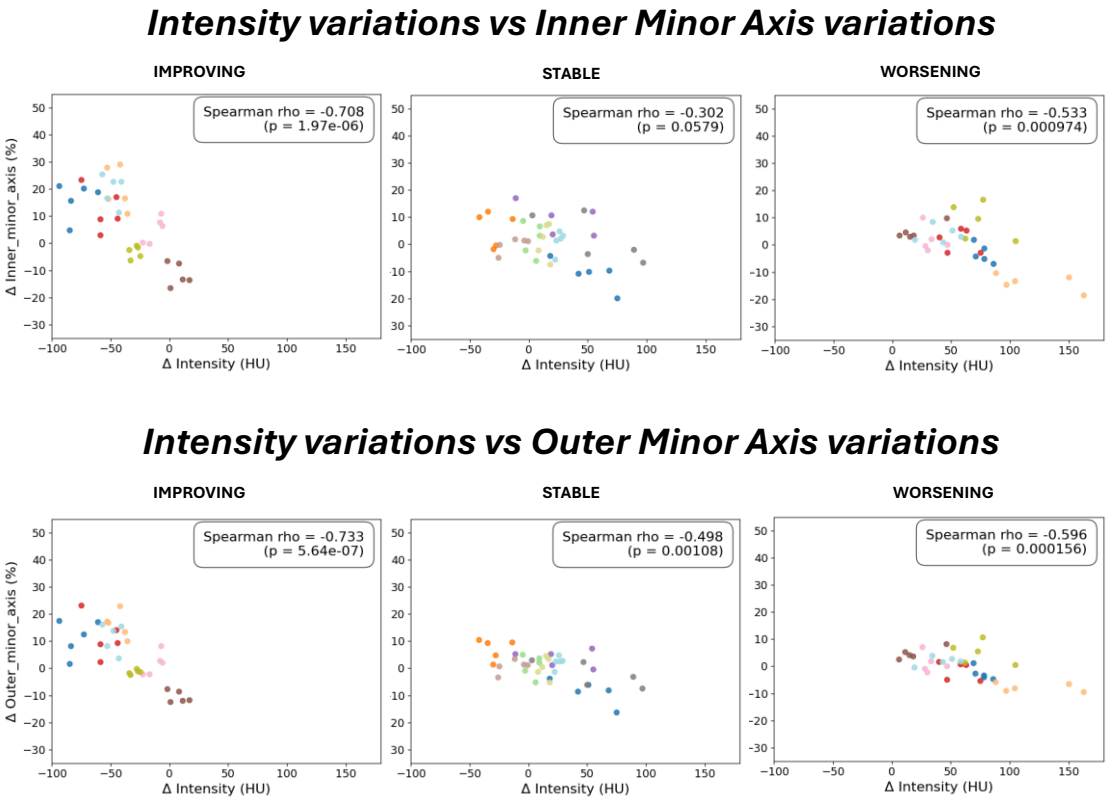

Figure 3.13 - Plots representing the relationship between the variations of axis dimensions and the variations of HU in the three different groups (Spearman coefficients are reported with their p-value): the dots with the same color are representing the different lobes of the same patient. Only minor axis measurements are shown as they are similar but much more significant than the major axis ones.

Results mirrored those observed for area measurements:

- The Improving group showed again a steep and significant inverse relationship.
- The Stable one had less pronounced axis variations with intensity variations.
- The Worsening group instead showed a stronger inverse relationship than the second group, but with a steepness lower than the first one, as happened in the areas' measurements.

4 Discussion and Conclusion

The presented pipeline was successfully applied to the standardized CHP dataset. The segmentation process produced consistent airway, lung and lobar masks. Minor corrections were needed to improve robustness, including a distal shift of the measurement point and pruning on the skeletonization of the trachea segment that sometimes had little spurious branches.

The validated registration process was applied on all the selected pairs of airway tree masks, and the estimated deformation fields were applied to the measurement points of the moving volumes. Correspondance between anatomical locations was established using a nearest-neighbor strategy, and longitudinal variations in geometrical features were computed. Each longitudinal pair was classified according to ΔFVC (Improving, Stable, Worsening). Parenchymal density analysis was integrated with geometrical analysis to evaluate structural remodeling patterns, both at global and local levels.

Global findings. From a global point of view, a clear separation of the three FVC-based groups was observed in terms of ΔHU, confirming the consistency between functional and densitometric metrics. Improving subjects exhibited predominantly negative ΔHU (density decrease) stable patients showed values centered around zero, and worsening subjects demonstrated positive ΔHU (density increase). The relationship between ΔFVC and ΔHU was non-linear, with a stronger negative association in

worsening subjects, suggesting that structural deterioration may have a stronger functional impact than structural improvement.

Global airway geometrical variations didn't significantly differentiate the three groups. This likely reflects disease heterogeneity, that makes some regions of the lungs more affected by a specific pattern, while others are more affected by different ones, and also regions trying to compensate for functional loss.

Regional findings. The local analysis has been done at lobar level. A clear association between density variation and airway remodeling became evident, particularly in the Improving group. A strong inverse correlation was observed: decreasing density was associated with increasing airway areas and axis dimensions. This suggests that airway expansion may accompany a decrease of lung inflammation, while fibrotic remodeling is mainly not reversible. Notably, these geometrical changes were observed even in the presence of relatively small ΔFVC values. This indicates that quantitative airway analysis may be more sensitive than a spirometry.

In the Stable group, both density and geometrical variations were centered around zero, and correlations were weak, indicating limited structural remodeling over time. The Worsening group showed a more complex pattern. Increases in density were associated with mixed airway responses: in some cases, airway dimensions decreased, consistent with progressive fibrotic narrowing; in others modest airway enlargement was observed, possibly reflecting traction bronchiectasis secondary to fibrosis.

Limitations of the study

Several limitations must be acknowledged.

First, the dataset was limited, preventing stratification by baseline disease severity. Patients differed substantially in baseline FVC and lung density, which may have influenced patterns of remodeling. The CHP patients in the dataset were all quite

different from each other and the stage of the pathology could vary a lot. Unfortunately, the dataset was limited in the number of subjects, so it wasn't possible to create several subsets with comparable starting levels of FVC and lung intensity and analyse the Improving, Stable and Worsening groups in those separate subsets.

Third, minor variability is acquisition parameters, such as in-plane resolution and temporal distances between image acquisitions and spirometry may have introduced additional variability.

Finally, regional analysis was performed at the lobar level. Although this improves global metrics lobes remain relatively large anatomical regions that may still contain heterogeneous pathological patterns. Multiple patterns could be present and impact on the included airways in a different way, leading to a mean change of geometrical features averaged within that region. A segmental approach could provide finer resolution of remodelling.

Methodological limitations

Other than the dataset issues, methodological aspects also present limitations.

The airway segmentation model was selected based on qualitative superiority. A future quantitative evaluation and comparison with the winning model of the AIIB 2023 challenge, trained on fibrotic datasets, would probably produce more reliable results.

The airway measurement algorithm instead evaluates discrete points along each branch. While effective, this approach may not fully capture branch-wide remodelling. Future developments could include branch-level summary statistics, including also minimum and maximum dimensions.

The registration algorithm was validated using coarser reconstructions. Although this was appropriate for validation, real-world variability in segmentation depth may still

influence correspondence in distal regions. Nonetheless, unmatched distal branches do not directly affect the matching of corresponding measurement points.

Conclusions

The proposed pipeline provides a reproducible framework for longitudinal quantitative airway analysis in CHP. Global lung density variations clearly separate Improving, Stable, and Worsening subjects. In contrast, global geometric metrics alone were insufficient to separate groups. However, at the regional level, meaningful associations between density variation and airway remodeling emerged.

Improving patients generally displayed enlargement in airway dimensions associated with density reduction. Stable patients showed minimal structural variation. Worsening patients exhibited mixed remodelling trends, with some dimensions increasing at lower intensity changes and decreasing at higher density increases. These results suggest that densitometric and geometrical descriptors capture complementary aspects of disease progression and their integration may characterize different disease trajectories.

Future work should focus on expanding the dataset to include a larger number of patients and a broader range of baseline FVC values. Such an expansion would enable stratified analyses across more homogeneous baseline subgroups, improving the interpretation of remodelling phenotypes and their clinical significance. In addition, pattern-recognition and machine learning approaches could support a more systematic identification of latent trajectories and improve the quality of group-level and subject-level findings.

More broadly, the pipeline appears suitable for application beyond CHP, including other fibrotic lung diseases in which quantitative airway analysis may provide added

value. With appropriate adaptation and validation, it could support translational investigations, bridging preclinical and clinical settings, enabling quantitative comparison of airway remodeling across species and contributing to pharmacodynamic assessment in therapeutic development.

Bibliography

[1] H. Furusawa *et al.*, 'Chronic Hypersensitivity Pneumonitis, an Interstitial Lung Disease with Distinct Molecular Signatures', *Am J Respir Crit Care Med*, vol. 202, no. 10, pp. 1430–1444, Nov. 2020, doi: 10.1164/rccm.202001-0134OC.

[2] L. Aliboni *et al.*, 'A Convolutional Neural Network Approach to Quantify Lung Disease Progression in Patients with Fibrotic Hypersensitivity Pneumonitis (HP)', *Academic Radiology*, vol. 29, no. 8, pp. e149–e156, Aug. 2022, doi: 10.1016/j.acra.2021.10.005.

[3] M. Zhang *et al.*, 'Multi-site, Multi-domain Airway Tree Modeling', *Medical Image Analysis*, vol. 90, p. 102957, Dec. 2023, doi: 10.1016/j.media.2023.102957.

[4] J. Wasserthal *et al.*, 'TotalSegmentator: Robust Segmentation of 104 Anatomic Structures in CT Images', *Radiology: Artificial Intelligence*, vol. 5, no. 5, p. e230024, Sep. 2023, doi: 10.1148/ryai.230024.

[5] L. Friedman, 'Respiratory System: Organs and its Functions'.

[6] J. A. Law and G. Kovacs, 'Airway Physiology and Anatomy'.

[7] A. Patwa and A. Shah, 'Anatomy and physiology of respiratory system relevant to anaesthesia', *Indian J Anaesth*, vol. 59, no. 9, p. 533, 2015, doi: 10.4103/0019-5049.165849.

[8] R. L. Johnson and C. C. W. Hsia, 'Anatomy and physiology of the human respiratory system', in *WIT Transactions on State of the Art in Science and Engineering*, 1st edn, vol. 1, V. Kulish, Ed., WIT Press, 2006, pp. 1–29. doi: 10.2495/978-1-85312-944-5/01.

[9] The Ohio State University Wexner Medical Center, 'Types of Lung Disease', Oct. 2016.

[10] M. Hamblin, H. Prosch, and M. Vašáková, 'Diagnosis, course and management of hypersensitivity pneumonitis', *Eur Respir Rev*, vol. 31, no. 163, p. 210169, Mar. 2022, doi: 10.1183/16000617.0169-2021.

[11] O. M. Dias *et al.*, 'Computed tomography in hypersensitivity pneumonitis: main findings, differential diagnosis and pitfalls', *Expert Review of Respiratory Medicine*, vol. 12, no. 1, pp. 5–13, Jan. 2018, doi: 10.1080/17476348.2018.1395282.

[12] M. Selman, A. Pardo, and T. E. King, 'Hypersensitivity Pneumonitis: Insights in Diagnosis and Pathobiology', *Am J Respir Crit Care Med*, vol. 186, no. 4, pp. 314–324, Aug. 2012, doi: 10.1164/rccm.201203-0513CI.

[13] M. Vasakova, F. Morell, S. Walsh, K. Leslie, and G. Raghu, 'Hypersensitivity Pneumonitis: Perspectives in Diagnosis and Management', *Am J Respir Crit Care Med*, vol. 196, no. 6, pp. 680–689, Sep. 2017, doi: 10.1164/rccm.201611-2201PP.

[14] M. Vasakova, M. Selman, F. Morell, M. Sterclova, M. Molina-Molina, and G. Raghu, 'Hypersensitivity Pneumonitis: Current Concepts of Pathogenesis and Potential Targets for Treatment', *Am J Respir Crit Care Med*, vol. 200, no. 3, pp. 301–308, Aug. 2019, doi: 10.1164/rccm.201903-0541PP.

[15] P. Spagnolo *et al.*, 'Hypersensitivity Pneumonitis: A Comprehensive Review', 2015.

[16] Y. Lacasse and Y. Cormier, 'Hypersensitivity pneumonitis', *Orphanet J Rare Dis*, vol. 1, no. 1, p. 25, Dec. 2006, doi: 10.1186/1750-1172-1-25.

[17] A. W. Creamer and S. L. Barratt, 'Prognostic factors in chronic hypersensitivity pneumonitis', *Eur Respir Rev*, vol. 29, no. 156, p. 190167, Jun. 2020, doi: 10.1183/16000617.0167-2019.

[18] S. K. Rajan *et al.*, 'Progressive pulmonary fibrosis: an expert group consensus statement', *Eur Respir J*, vol. 61, no. 3, p. 2103187, Mar. 2023, doi: 10.1183/13993003.03187-2021.

[19] P. Canivet and E. Coche, 'Lung Fibrosis on CT Imaging: Essentials and Updates', *Journal of the Belgian Society of Radiology*, vol. 108, no. 1, p. 100, 2024, doi: 10.5334/jbsr.3775.

[20] A. G. Brixey and B. M. Elicker, 'Clinical Indications for High-Resolution Chest CT'.

[21] P. Whiting, N. Singatullina, and J. Rosser, 'Computed tomography of the chest: I. Basic principles', *BJA Education*, vol. 15, no. 6, pp. 299–304, Dec. 2015, doi: 10.1093/bjaceaccp/mku063.

[22] European Society of Radiology (ESR), H. Almansour, J. Brendel, and D. Wessling, 'Modern Radiology eBook: Computed Tomography', M. Becker, Ed., European Society of Radiology, 2024. doi: 10.26044/ESR-MODERN-RADIOLOGY-04.

[23] S. L. F. Walsh, N. Sverzellati, A. Devaraj, A. U. Wells, and D. M. Hansell, 'Chronic hypersensitivity pneumonitis: high resolution computed tomography patterns

and pulmonary function indices as prognostic determinants', *Eur Radiol*, vol. 22, no. 8, pp. 1672–1679, Aug. 2012, doi: 10.1007/s00330-012-2427-0.

[24] M. S. Wilson and T. A. Wynn, 'Pulmonary fibrosis: pathogenesis, etiology and regulation', *Mucosal Immunology*, vol. 2, no. 2, pp. 103–121, Mar. 2009, doi: 10.1038/mi.2008.85.

[25] A. Bekki1, T. Beauperthuy1, and M. Ángel Martínez-García1,2, 'Traction bronchiectasis: is it as benign as we think?', *J Bras Pneumol.*, p. e20220220, Aug. 2022, doi: 10.36416/1806-3756/e20220220.

[26] H. Barnes *et al.*, 'Diagnosis and management of hypersensitivity pneumonitis in adults: A position statement from the Thoracic Society of Australia and New Zealand', *Respirology*, vol. 29, no. 12, pp. 1023–1046, Dec. 2024, doi: 10.1111/resp.14847.

[27] M. Wijsenbeek and V. Cottin, 'Spectrum of Fibrotic Lung Diseases', *N Engl J Med*, vol. 383, no. 10, pp. 958–968, Sep. 2020, doi: 10.1056/NEJMra2005230.

[28] M. Roman Rodriguez and Cimas, '"Quick guide to spirometry," IPCRG Desktop Helper, no. 14. [Online].' Apr. 2023. [Online]. Available: https://www.ipcrg.org/dth14

[29] *National Asthma Council Australia, The spirometry handbook for primary care. Melbourne: National Asthma Council Australia, Mar. 2023.*

[30] J. Choe, E. J. Chae, Y. J. Kim, K.-H. Do, J. S. Song, and J. W. Song, 'Serial changes of CT findings in patients with chronic hypersensitivity pneumonitis: imaging trajectories and predictors of fibrotic progression and acute exacerbation', *Eur Radiol*, vol. 31, no. 6, pp. 3993–4003, Jun. 2021, doi: 10.1007/s00330-020-07469-2.

[31] P. Lo *et al.*, 'Extraction of Airways From CT (EXACT'09)', *IEEE Trans. Med. Imaging*, vol. 31, no. 11, pp. 2093–2107, Nov. 2012, doi: 10.1109/TMI.2012.2209674.

[32] Y. Nan *et al.*, 'Hunting imaging biomarkers in pulmonary fibrosis: Benchmarks of the AIIB23 challenge', *Medical Image Analysis*, vol. 97, p. 103253, Oct. 2024, doi: 10.1016/j.media.2024.103253.

[33] D. S. Carmo *et al.*, 'MEDPSeg: Hierarchical polymorphic multitask learning for the segmentation of ground-glass opacities, consolidation, and pulmonary structures on computed tomography', Mar. 25, 2024, *arXiv*: arXiv:2312.02365. doi: 10.48550/arXiv.2312.02365.

[34] C. Mascheroni, 'Automatic measurement of airway dimensions from CT images in health and asthma', Politecnico di Milano, 2022.

[35] J. Tschirren, E. A. Hoffman, G. McLennan, and M. Sonka, 'Intrathoracic airway trees: segmentation and airway morphology analysis from low-dose CT scans',

IEEE Trans. Med. Imaging, vol. 24, no. 12, pp. 1529–1539, Dec. 2005, doi: 10.1109/TMI.2005.857654.

[36] M. Patyk, A. Obojski, D. Sokołowska-Dąbek, M. Parkitna-Patyk, and U. Zaleska-Dorobisz, 'Airway wall thickness and airflow limitations in asthma assessed in quantitative computed tomography', *Ther Adv Respir Dis*, vol. 14, p. 1753466619898598, Jan. 2020, doi: 10.1177/1753466619898598.

[37] J. M. Fitzpatrick, D. L. G. Hill, and C. R. Maurer, 'CHAPTER 8 Image Registration'.

[38] A. Sotiras, C. Davatzikos, and N. Paragios, 'Deformable Medical Image Registration: A Survey', *IEEE Trans. Med. Imaging*, vol. 32, no. 7, pp. 1153–1190, Jul. 2013, doi: 10.1109/TMI.2013.2265603.

[39] D. Rueckert, L. I. Sonoda, C. Hayes, D. L. G. Hill, M. O. Leach, and D. J. Hawkes, 'Nonrigid registration using free-form deformations: application to breast MR images', *IEEE Trans. Med. Imaging*, vol. 18, no. 8, pp. 712–721, Aug. 1999, doi: 10.1109/42.796284.

[40] T. Vercauteren, X. Pennec, A. Perchant, and N. Ayache, 'Diffeomorphic demons: Efficient non-parametric image registration', *NeuroImage*, vol. 45, no. 1, pp. S61–S72, Mar. 2009, doi: 10.1016/j.neuroimage.2008.10.040.

[41] Nata SC, Launico MV. Anatomy, Airway. [Updated 2025 Sep 15]. In: StatPearls [Internet]. Treasure Island (FL): StatPearls Publishing; 2025 Jan-. Available from: https://www.ncbi.nlm.nih.gov/books/NBK459258/

[42] Chandra D, Cherian SV. Hypersensitivity Pneumonitis. [Updated 2023 Jul 10]. In: StatPearls [Internet]. Treasure Island (FL): StatPearls Publishing; 2025 Jan-. Available from: https://www.ncbi.nlm.nih.gov/books/NBK499918/

[a] https://www.stanfordchildrens.org/en/topic/default?id=anatomy-of-the-respiratory-system-85-P01300

[b] https://training.seer.cancer.gov/anatomy/respiratory/passages/

[c] https://thoracickey.com/overview-of-the-respiratory-system-function-and-structure/

[d] https://pulmonarypracticeassociates.com/lung-disease/

[e] http://www.mychox.net/cf/imaging.php

[f] https://atm22.grand-challenge.org/

[g] https://psnet.ahrq.gov/web-mm/one-bronchoscopy-two-errors

[h] https://www.radiology.expert/en/modules/xrayct-technique/types-of-ct-techniques/

[i] https://github.com/EndoluminalSurgicalVision-IMR/ATM-22-Related-Work/tree/main/ATM22-Challenge-Top5-Solution/team_yanglab

List of Figures

List of Tables

Acknowledgments

I would like to sincerely thank Professor Pennati and Professor Aliverti for their availability and for the invaluable support they provided throughout this work. Their guidance, insight, and encouragement were essential at every stage of the project.

I am also deeply grateful to my parents for their constant love and support. A heartfelt thank you goes to my sisters for always being by my side. Finally, I would like to thank my grandmothers for their warmth, patience, and unwavering faith in me.